

Topography of Spin Liquids on a Triangular Lattice

Zhenyue Zhu,¹ P. A. Maksimov,¹ Steven R. White,¹ and A. L. Chernyshev¹

¹*Department of Physics and Astronomy, University of California, Irvine, California 92697, USA*

(Dated: May 11, 2018)

Spin systems with frustrated anisotropic interactions are of significant interest due to possible exotic ground states. We have explored their phase diagram on a nearest-neighbor triangular lattice using the density-matrix renormalization group and mapped out the topography of the region that can harbor a spin liquid. We find that this spin-liquid phase is continuously connected to a previously discovered spin-liquid phase of the isotropic J_1 – J_2 model. The two limits show nearly identical spin correlations, making the case that their respective spin liquids are isomorphic to each other.

Some of the most visionary ideas prevail despite failing the original test case they were suggested to describe. Such is the seminal proposal of a spin liquid (SL) as a ground state of the nearest-neighbor (NN) $S = \frac{1}{2}$ triangular-lattice (TL) Heisenberg antiferromagnet [1]. Although the ground state of this model proved to be magnetically ordered [2, 3], the concept of spin liquid remains highly influential in a much broader context [4, 5].

The recent surge of activity [6–29] brings back the NN TL model as a potential holy grail of spin liquids that may provide a redemption to the original proposal of Ref. [1]. In its modern reincarnation, the key players are the highly anisotropic spin interactions, borne out of the strong spin-orbit coupling [6, 8, 25]. This ongoing effort is also inspired by the Kitaev SL construct for the bond-dependent spin interactions on the honeycomb lattice [30], although without the benefit of an exact solution in the TL geometry.

The highly anisotropic interactions naturally emerge from a projection of the large magnetic moments' Hilbert space onto the manifold of low-energy pseudospin- $\frac{1}{2}$ degrees of freedom of the rare-earth compounds [8, 31]. Among the recently discovered TL rare-earth-based magnets, YbMgGaO₄ (YMGO) [6] has received most attention. While the debate on the intrinsic vs disorder-induced nature of its spin-liquid-like response is ongoing [6, 7, 16, 18, 26, 27], a broader family of the rare-earth TL materials has also become available [8, 29].

Thus, it is important to provide a much needed framework to this area by establishing the phase diagram of the most general NN TL model with an unbiased numerical approach that goes beyond the mean-field methods that favor SL by design [7, 11]. That should also settle whether extrinsic mechanisms are at work to mimic an SL behavior in the cases such as YMGO [16].

In this Letter, we explore the three-dimensional (3D) phase diagram of the most general NN model of these materials by using the density-matrix renormalization group (DMRG) aided by quasiclassical analysis. In agreement with prior numerical work [16, 17, 25], we find that the phase diagram is dominated by well-ordered states and shows no indication that anisotropic terms by themselves can lead to a massive degeneracy that can favor SL states. On the contrary, most of the phase boundaries are sur-

prisingly close to that of the classical $S = \infty$ limit, implying reduced quantum fluctuations and strongly gapped states due to anisotropies.

Nonetheless, we have found a likely candidate for an SL state and created its topographic map, although a weak or a more complicated ordering [9] cannot be fully ruled out for much of that region. The maximal extent of the SL phase is achieved at the isotropic limit of the bond-independent part of the model, questioning that anisotropies are a prime source of an SL in these systems.

While the local character of the f -shell magnetism of the rare-earth ions dictates the dominance of the NN interactions, experiments suggest a sizable next-NN coupling J_2 [12, 24]. We find that a four-dimensional extension of the phase diagram with J_2 allows for a natural continuity of the SL state from the anisotropic TL to the isotropic J_1 – J_2 limit [32–41]. The spin-spin correlations show no transition vs J_2 and are nearly identical between these two limits, suggesting isomorphism of the corresponding SL states. Our study indicates that these SLs are either Z_2 or Dirac-like [25, 34–41], not the “spinon metal” SL state, argued to exist in YMGO [7, 23].

Model.—The general NN TL model [6, 8] with spin anisotropies constrained by the TL symmetries has both XXZ and bond-dependent terms, $\mathcal{H} = \mathcal{H}_{XXZ} + \mathcal{H}_{\text{bd}}$,

$$\begin{aligned}\mathcal{H}_{XXZ} &= J \sum_{\langle ij \rangle} (S_i^x S_j^x + S_i^y S_j^y + \Delta S_i^z S_j^z), \\ \mathcal{H}_{\text{bd}} &= \sum_{\langle ij \rangle} 2J_{\pm\pm} \left(\cos \tilde{\varphi}_\alpha [x, y]_{ij} - \sin \tilde{\varphi}_\alpha \{x, y\}_{ij} \right) \\ &\quad + J_{z\pm} \left(\cos \tilde{\varphi}_\alpha \{y, z\}_{ij} - \sin \tilde{\varphi}_\alpha \{x, z\}_{ij} \right),\end{aligned}\quad (1)$$

where $0 \leq \Delta \leq 1$ for layered systems, auxiliary phases are $\tilde{\varphi}_\alpha = \{0, -2\pi/3, 2\pi/3\}$ for bonds along the primitive vectors $\tilde{\delta}_\alpha$ in Fig. 1, and notations $[a, b]_{ij} = S_i^a S_j^a - S_i^b S_j^b$ and $\{a, b\}_{ij} = S_i^a S_j^b + S_i^b S_j^a$ are used for brevity [42].

Classical phase diagram.—The XXZ term in (1) favors coplanar states: the well-known 120° state for $\Delta \leq 1$ and $J > 0$, and a ferromagnetic state for $J < 0$. The terms in \mathcal{H}_{bd} in (1) result in trends that are incompatible for different bonds [43], leaving no continuous spin symmetries and selecting “stripe- \mathbf{x} ” and “stripe- \mathbf{yz} ” as classical ground states [6, 8, 17]; see Fig. 1.

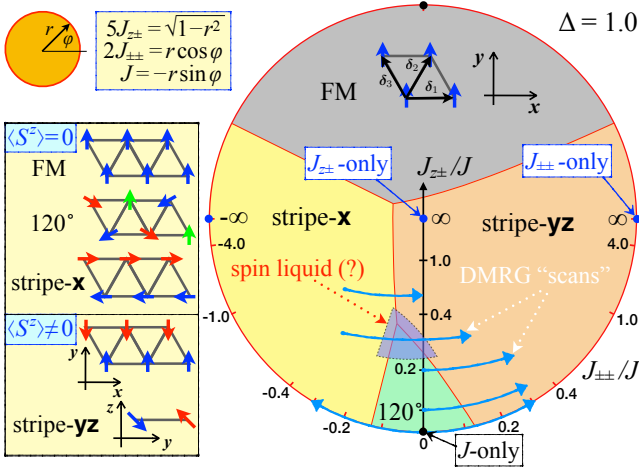


FIG. 1: The classical 2D phase diagram of the model (1) for $\Delta = 1.0$ using polar parametrization (see inset). The sketches of the ordered states (see text) and lattice primitive vectors are shown. Some of the DMRG scans of Figs. 2 and 3 are shown by arrows. The shaded triangle shows the SL phase. For the 3D phase diagram and phase boundaries see SM [43]

In the “stripe-x” state, favored by $J_{\pm\pm} < 0$, spins align along one bond in ferromagnetic “stripes” that order antiferromagnetically, see Fig. 1. This structure is only partially frustrated as the $J_{\pm\pm}$ term is fully satisfied on the x -bond and half-satisfied on two other bonds [17, 43]. The “stripe-yz” state benefits the $J_{\pm\pm} > 0$ and $J_{z\pm}$ terms in a similar manner. Here spins in ferromagnetic stripes are perpendicular to the fully satisfied x -bond and are tilting out of the lattice plane with the angle dependent on the ratio $J_{z\pm}/J_{\pm\pm}$, reaching $\pi/4$ at $J_{z\pm} \rightarrow \infty$ [17]. The boundaries between all phases in Fig. 1 can be found analytically; see the Supplemental Material (SM), Ref. [43]. The results are identical for $J_{z\pm} < 0$ [8].

In Fig. 1, we present a two-dimensional (2D) cut of the classical 3D phase diagram of the NN TL model (1) at $\Delta = 1.0$ that shows all four phases discussed above. The full 3D phase diagram is a solid cylinder with the vertical axis $0 \leq \Delta \leq 1$ and the 2D cuts showing only quantitative changes vs Δ ; see the SM [43]. The polar parametrization maps the 2D parameter space onto a circle and the choice of numerical factors is to exaggerate the region $J_{\pm\pm}, J_{z\pm} \lesssim J$. In Fig. 1, we also identify an area of the suspected SL phase discussed below. It has a similarly limited extent along the Δ -axis of the 3D phase diagram.

DMRG results.—To investigate the 3D phase diagram of the model (1) by DMRG we use several complementary approaches. First is the long-cylinder 1D “scans,” in which one of the parameters is varied along the length of the cylinder and spin patterns provide a faithful visual extent of different phases that appear [16, 34, 45]. We use different boundary conditions and ranges of the varied parameter to exclude unwanted proximity effects [43]. Second are the shorter cylinders [46] with fixed parameters [“non-scans”] used as a probe for a sequence of

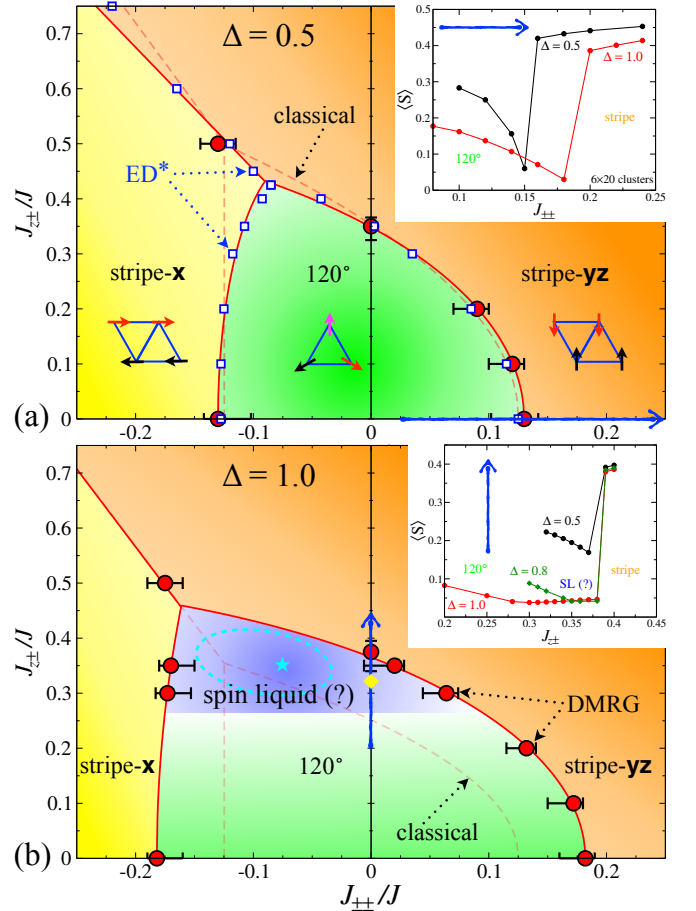


FIG. 2: The 2D phase diagrams for $\Delta = 0.5$ and 1.0 . The circles are from the 1D DMRG scans, see text and Fig. 3, squares are ED results [17], solid lines are guides to the eye, dashed lines are classical phase boundaries, arrows show parameter cuts for the insets. Insets show $\langle S \rangle$ vs $J_{\pm\pm}$ ($J_{z\pm}$) in units of J from cylinders with fixed parameters [46]. Stars are parameters used in $1/L$ scaling in Fig. 3(c), see text.

points along the same 1D scans or at individual points of the phase diagram. Third is the $1/L$ scaling of the ordered moment using clusters with fixed aspect ratio [3]. We also use measurements of the correlation lengths and intensity maps of the structure factor, $\mathcal{S}(\mathbf{q})$ [43].

Figs. 2 and 3 present our key results; see the SM [43] for details. In Fig. 2 we show 2D phase diagrams for $\Delta = 0.5$ and 1.0 , focusing on the region around the 120° phase. The circles with error bars are transitions observed in the scans, such as the ones shown in Figs. 3(a) and (b); squares in Fig. 2(a) are the exact-diagonalization (ED) results from Ref. [17]; solid lines are guides to the eye.

Our scans for $\Delta = 0.5$ in Fig. 2(a) and the ED are remarkably close, both showing direct transitions between robust magnetic orders that are nearly coincident with the classical phase boundaries (dashed lines). The non-scan ordered moments, shown in the insets of Fig. 2 along two representative cuts, support these findings.

Fig. 2(b) summarizes our results for the isotropic limit of the XXZ term (1), $\Delta = 1.0$. We find an expansion of

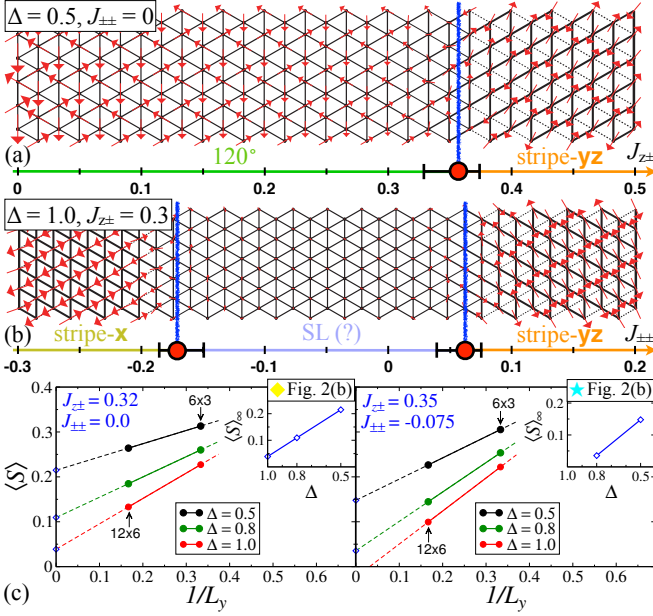


FIG. 3: The 1D DMRG scans [46] for (a) $\Delta = 0.5$, $J_{\pm\pm} = 0$ vs $J_{z\pm}$, and (b) $\Delta = 1.0$, $J_{z\pm} = 0.3$ vs $J_{\pm\pm}$ [$J_{\pm\pm}$, $J_{z\pm}$ in units of J]. The circles and lines show transitions, arrows are the in-plane projections of $\langle S \rangle$. (c) The $1/L$ scaling of $\langle S \rangle$ for parameters marked with stars in Fig. 2(b). Insets show Δ -dependencies of the extrapolated $\langle S \rangle_\infty$.

the 120° phase beyond its classical boundaries with the transitions from it to the stripe phases remaining direct for $J_{z\pm} \lesssim 0.25$ [43]; see inset in Fig. 2(a). Here we find a possible SL state in the $J_{z\pm} \simeq [0.27, 0.45]$ window; see also Fig. 3(b) and SM [43].

The inset of Fig. 2(b) presents the non-scan ordered moment $\langle S \rangle$ along the $J_{z\pm}$ cut. It shows a kink-like feature at $J_{z\pm} \approx 0.28$ for $\Delta = 1.0$. However, the intermediate phase from $J_{z\pm} \approx 0.28$ to 0.38 still exhibits a weak order. The same plot shows a similar feature for $\Delta = 0.8$ from $J_{z\pm} \approx 0.35$ to 0.38 while for $\Delta = 0.5$ the transition is direct. The scans for $\Delta = 0.8$ show the SL-suspect region that is significantly smaller than for $\Delta = 1.0$ [43]. We note that all transitions to stripe states that we observe are first-order like.

Another test of the SL region is provided by the $1/L$ scaling of the ordered moment $\langle S \rangle$ [3] in Fig. 3(c) for representative points indicated by the stars in Fig. 2(b). The insets of Fig. 3(c) show the Δ -dependence of the extrapolated moment $\langle S \rangle_\infty$. This analysis suggests an SL state in a significantly smaller 3D region than the long-cylinder scans. Its approximate extent in $\Delta = 1.0$ plane is shown in Fig. 2(b) by the dashed oval and it is limited along the XXZ axis by $\Delta \gtrsim 0.9$.

This should be compared with the J_1 - J_2 model, where different methods used here agree very closely on the extent of the SL region [16, 34, 43]. This is not the case in the present study, suggesting that a weak and/or more complicated form ordering [9] may persist in much of the suspected SL region.

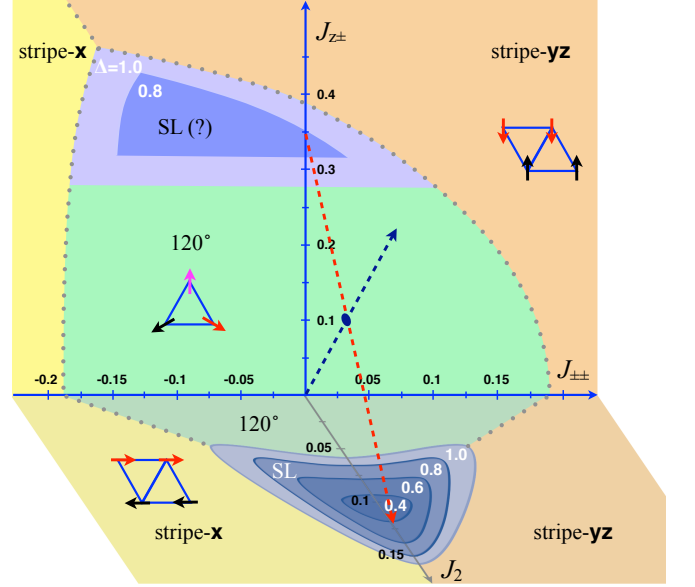


FIG. 4: Topographic maps of the SL regions of the 3D phase diagrams of the NN ($J_2 = 0$) model (1) [back panel] and of the J_1 - J_2 - $J_{\pm\pm}$ ($J_{z\pm} = 0$) XXZ model [16] [lower panel]. Δ -cuts are given in 0.2 increments and indicated. Dashed arrows show 1D DMRG cuts in Fig. 5.

We also verified that larger anisotropies enhance magnetic order and imply strongly gapped states, confirmed by the quasiclassical analysis [43]. One parameter choice that shows a nearly classical stripe order [47] was originally advocated as a suitable SL for YMGO [13, 21].

We summarize the 3D quantum phase diagram for the model (1) in the back panel of Fig. 4 as a topographic map. It retains all classical phases of Fig. 1 and acquires an SL region. The generous outline of the latter represents a distorted cone-like shape with the base at $\Delta = 1.0$ and the widest dimensions $J_{z\pm} \simeq [0.27, 0.45]$ and $J_{\pm\pm} \simeq [-0.17, 0.1]$ at that base. The tip of the cone extends along the XXZ axis down to $\Delta \gtrsim 0.7$. As is discussed above, the actual SL region may be significantly smaller. We also note that the SL phase occurs within the 120° region and its maximal extent is achieved at the isotropic limit of the XXZ term, questioning the importance of anisotropies for its existence.

J_2 -extension.—Some of the most reliable experiments in YMGO strongly suggest that one should add a second-NN J_2 -term to the NN model (1) [12, 24]. The isotropic J_1 - J_2 model is also known to have an SL state for a range of $J_2 \approx [0.06, 0.16]J_1$ [33–41]. For both reasons, a minimal modification of the NN model (1) by the XXZ -only next-NN J_2 -term suffices [43].

Recently, we have investigated the effect of the XXZ and $J_{\pm\pm}$ anisotropic terms on the J_1 - J_2 SL phase [16]. It survives down to $\Delta \approx 0.3$ and is eliminated completely by $|J_{\pm\pm}| \approx 0.1$. In the bottom panel of Fig. 4, we present a topographic map of the SL state in this XXZ J_1 - J_2 - $J_{\pm\pm}$ ($J_{z\pm} = 0$) model using results from Ref. [16].

Fig. 4 suggests a connection between the SL phases

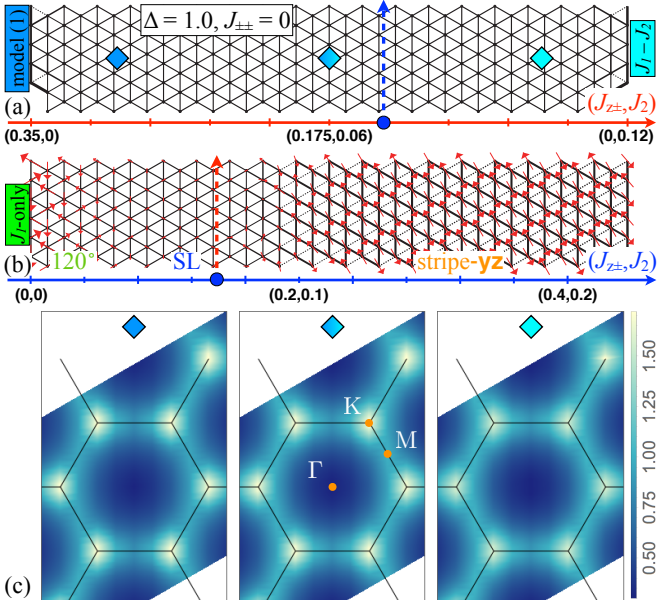


FIG. 5: (a) and (b) DMRG scans at $\Delta = 1.0$ as shown in Fig. 4. $J_{z\pm}$, J_2 are in units of J_1 ; the crossing point of the scans in Fig. 4 is shown by blue dots and dashed arrows. (c) $S(\mathbf{q})$ maps from three section of the cylinder in (a) marked by the diamonds.

of the anisotropic model (1) and of its isotropic J_1 - J_2 counterpart. We verify this connection for $\Delta = 1.0$ where the extent of both SL regions in Fig. 4 is maximal. We use two long-cylinder DMRG scans in the $J_{\pm\pm} = 0$ plane shown in Fig. 4 by arrows. The first scan connects the anisotropic SL at $J_{z\pm} = 0.35$ with the isotropic J_1 - J_2 SL at $J_2 = 0.12$ (units of J_1). The second scan starts at the origin (J_1 -only model) and is used to confirm the existence of an SL state between the 120° and the stripe phases along the direction tilted from the J_2 and $J_{z\pm}$ axes. For a different picture of these cuts, see SM [43].

Figs. 5(a) and (b) show the real-space images of these scans; dashed arrows are marking their crossing point; both coordinates $(J_{z\pm}, J_2)$ are indicated. The first cylinder has open boundary condition and one site removed at each end to suppress spinon localization at the edge [34, 43]. The scan shows no indication of magnetic, chiral, or valence-bond order [43] and no change of the SL state along the cylinder, the latter inferred from the thickness of the bonds that are proportional to the nearest-neighbor correlation $\langle \mathbf{S}_i \mathbf{S}_j \rangle$. The second scan, Fig. 5(b), shows a transition from the 120° to the stripe- \mathbf{yz} state via an intermediate SL state, consistent with the first scan and also with the results in Fig. 2(b) and Fig. 4 and in Refs. [16, 43] for the scans of the same nature along $J_{z\pm}$ and J_2 axes.

To infer the character of the SL states, we calculate the static structure factor, $S(\mathbf{q})$, using correlations from the three section of the cylinder in Fig. 5(a) with centers of these sections marked by the diamonds [48]. The first section represents the region that is close to the limit

of the original anisotropic model (1), the third section is close to the isotropic J_1 - J_2 SL, and the second is in between. The results are shown in Fig. 5(c) where $S(\mathbf{q})$ is at $q_z = 0$ [49]. We have also calculated $S(\mathbf{q})$ in non-scan cylinders for the limits of the scan in Fig. 5(a) as well as at other points within the SL regions in Fig. 4 with quantitatively very similar results [43].

The structure factors in Fig. 5(c) are nearly identical, implying that the SLs in the anisotropic model (1) and in the isotropic J_1 - J_2 model, as well as any SL state in between, are isomorphic to each other [50]. The correlations show a broadened peak at the K -points, the feature consistent with the Z_2 [34–36], $U(1)$ Dirac [37], or Dirac-like [25, 38–41] SLs, but not with the spinon Fermi surface SL state proposed for YMGO [7, 23]. This suggests that an extrinsic mechanism is responsible for an SL-like response in this material. The YMGO structure factor has maxima of intensity at the M -points, the feature readily obtainable from stripe domains of mixed orientations, see [43], supporting the SL mimicry scenario of Ref. [16].

Summary.—We have explored the 3D phase diagram of the anisotropic NN model on an ideal TL lattice (1) using DMRG approaches. In agreement with prior work, well-ordered states dominate most of it, showing reduced quantum fluctuations and strongly gapped states for significant anisotropic interactions, also confirmed by the quasiclassical analysis. We have identified an SL region of the phase diagram and created its topographic map. This SL state occurs at the border between 120° and stripe phases, with its maximal extent reached at the isotropic limit of the XXZ term. We have studied a four-dimensional extension of the phase diagram by the next-NN J_2 -term and have shown that it connects the newly found SL state to the well-known isotropic J_1 - J_2 model. The spin-spin correlations are nearly identical everywhere between these two limits, suggesting a complete isomorphism of the corresponding SL states. This also rules out the “spinon metal” SL state as a viable candidate for materials that realize anisotropic TL model. We also note that given its relative volume of the phase diagram, realizing the newly discovered SL state in a real material would require a parameter fine-tuning.

Acknowledgments.—We thank Prof. Xiaoqun Wang and Dr. Qiang Luo for sending their published data from Ref. [17], Itamar Kimchi for sharing his notes prior to publication and a discussion, and Cecile Repellin for sharing unpublished results and a useful conversation. We are grateful to George Jackeli for a patient discussion and support and to Natalia Perkins for a useful technical tip. We are indebted to Martin Mourigal for numerous communications, explanations, indispensable comments, and unique insights. This work was supported by the U.S. Department of Energy, Office of Science, Basic Energy Sciences under Award No. DE-FG02-04ER46174 (P. A. M. and A. L. C.) and by the NSF through grant DMR-1505406 (Z. Z. and S. R. W.).

-
- [1] P. W. Anderson, *Mater. Res. Bull.* **8**, 153 (1973); P. Fazekas and P. W. Anderson, *Philos. Mag.* **30**, 423 (1974).
- [2] L. Capriotti, A. E. Trumper, and S. Sorella, *Phys. Rev. Lett.* **82**, 3899 (1999).
- [3] S. R. White and A. L. Chernyshev, *Phys. Rev. Lett.* **99**, 127004 (2007).
- [4] L. Savary and L. Balents, *Rep. Prog. Phys.* **80**, 016502 (2017).
- [5] L. Balents, *Nature* **464**, 199 (2010).
- [6] Y. Li, H. Liao, Z. Zhang, S. Li, F. Jin, L. Ling, L. Zhang, Y. Zou, L. Pi, Z. Yang, J. Wang, Z. Wu, and Q. Zhang, *Scientific Reports* **5**, 16419 (2015).
- [7] Y. Li, G. Chen, W. Tong, Li Pi, J. Liu, Z. Yang, X. Wang, and Q. Zhang, *Phys. Rev. Lett.* **115**, 167203 (2015).
- [8] Y.-D. Li, X. Wang, and G. Chen, *Phys. Rev. B* **94**, 035107 (2016).
- [9] C. Liu, X. Wang, R. Yu, *Phys. Rev. B* **94**, 174424 (2016).
- [10] Y. S. Li, D. Adroja, P. K. Biswas, P. J. Baker, Q. Zhang, J. J. Liu, A. A. Tsirlin, P. Gegenwart, and Q. M. Zhang, *Phys. Rev. Lett.* **117**, 097201 (2016).
- [11] Y. Shen, Y.-D. Li, H. Wo, Y. Li, S. Shen, B. Pan, Q. Wang, H. C. Walker, P. Steffens, M. Boehm, Y. Hao, D. L. Quintero-Castro, L. W. Harriger, M. D. Frontzek, L. Hao, S. Meng, Q. Zhang, G. Chen, and J. Zhao, *Nature* **540**, 559 (2016).
- [12] J. A. M. Paddison, M. Daum, Z. Dun, G. Ehlers, Y. Liu, M. B. Stone, H. Zhou, and M. Mourigal, *Nat. Phys.* **13**, 117 (2017).
- [13] Y.-D. Li, Y. Shen, Y. Li, J. Zhao, and G. Chen, *arXiv:1608.06445*.
- [14] Y. Xu, J. Zhang, Y. S. Li, Y. J. Yu, X. C. Hong, Q. M. Zhang, and S. Y. Li, *Phys. Rev. Lett.* **117**, 267202 (2016).
- [15] Y. D. Li, Y.-M. Lu, and G. Chen, *Phys. Rev. B* **96**, 054445 (2017).
- [16] Z. Zhu, P. A. Maksimov, S. R. White, and A. L. Chernyshev, *Phys. Rev. Lett.* **119**, 157201 (2017).
- [17] Q. Luo, S. Hu, B. Xi, J. Zhao, and X. Wang, *Phys. Rev. B* **95**, 165110 (2017).
- [18] Y. Li, D. Adroja, R. I. Bewley, D. Voneshen, A. A. Tsirlin, P. Gegenwart, and Q. Zhang, *Phys. Rev. Lett.* **118**, 107202 (2017).
- [19] Y. D. Li and G. Chen, *Phys. Rev. B* **96**, 075105 (2017).
- [20] Y. Li, D. Adroja, D. Voneshen, R. I. Bewley, Q. Zhang, A. A. Tsirlin, and P. Gegenwart, *Nat. Commun.* **8**, 15814 (2017).
- [21] S. Tóth, K. Rolfs, A. R. Wildes, and C. Rüegg, *arXiv:1705.05699*.
- [22] Z.-X. Luo, E. Lake, J.-W. Mei, and O. A. Starykh, *arXiv:1706.01597*.
- [23] Y. Shen, Y.-D. Li, H. C. Walker, P. Steffens, M. Boehm, X. Zhang, S. Shen, H. Wo, G. Chen, and J. Zhao, *arXiv:1708.06655*.
- [24] X. Zhang, F. Mahmood, M. Daum, Z. Dun, J. A. M. Paddison, N. J. Laurita, T. Hong, H. Zhou, N. P. Armitage, and M. Mourigal, *arXiv:1708.07503*.
- [25] J. Iaconis, C. Liu, G. B. Halász, and L. Balents, *arXiv:1708.07856*.
- [26] Z. Ma, J. Wang, Z.-Y. Dong, J. Zhang, S. Li, S.-H. Zheng, Y. Yu, W. Wang, L. Che, K. Ran, S. Bao, Z. Cai, P. Čermák, A. Schneidewind, S. Yano, J. S. Gardner, X. Lu, S.-L. Yu, J.-M. Liu, S. Li, J.-X. Li, and J. Wen, *arXiv:1709.00256*.
- [27] I. Kimchi, A. Nahum, and T. Senthil, *arXiv:1710.06860*.
- [28] E. Parker and L. Balents, *arXiv:1801.06941*.
- [29] M. B. Sanders, F. A. Cevallos, and R. J. Cava, *Mater. Res. Express* **4**, 036102 (2017).
- [30] A. Kitaev, *Ann. Phys.* **321**, 2 (2006).
- [31] J. S. Gardner, M. J. P. Gingras, and J. E. Greedan, *Rev. Mod. Phys.* **82**, 53 (2010).
- [32] C. J. Gazza, and H. A. Ceccatto, *J. Phys.: Condens. Matter* **5**, L135 (1993).
- [33] P. H. Y. Li, R. F. Bishop, and C. E. Campbell, *Phys. Rev. B* **91**, 014426 (2015).
- [34] Z. Zhu and S. R. White, *Phys. Rev. B* **92**, 041105 (2015).
- [35] W.-J. Hu, S.-S. Gong, W. Zhu, and D. N. Sheng, *Phys. Rev. B* **92**, 140403 (2015).
- [36] D.-V. Bauer and J. O. Fjærestad, *arxiv: 1710.08720*.
- [37] Y. Iqbal, W.-J. Hu, R. Thomale, D. Poilblanc, and F. Becca, *Phys. Rev. B* **93**, 144411 (2016).
- [38] R. Kaneko, S. Morita, and M. Imada, *J. Phys. Soc. Jpn.* **83**, 093707 (2014).
- [39] S.-S. Gong, W. Zhu, J.-X. Zhu, D. N. Sheng, and K. Yang, *Phys. Rev. B* **96**, 75116 (2017).
- [40] S. N. Saadatmand and I. P. McCulloch, *Phys. Rev. B* **94**, 121111 (2016).
- [41] R. V. Mishmash, J. R. Garrison, S. Bieri, and C. Xu, *Phys. Rev. Lett.* **111**, 157203 (2013).
- [42] For a less humane form of (1), see, e.g., [7]. We use a standard form of the XXZ term (cf. [7] and others) with $J = 2J_{\pm}$ and anisotropy $\Delta = J_z/2J_{\pm}$ in their notations and a different operator form in \mathcal{H}_{bd} (1).
- [43] See Supplemental Material at <http://link.aps.org/supplemental/>, which includes Refs. [44], for technical details on the model, additional DMRG and spin-wave theory (SWT) results.
- [44] A. Biffin, R. D. Johnson, I. Kimchi, R. Morris, A. Bombardi, J. G. Analytis, A. Vishwanath, and R. Coldea, *Phys. Rev. Lett.* **113**, 197201 (2014).
- [45] Z. Zhu, D. A. Huse, and S. R. White, *Phys. Rev. Lett.* **110**, 127205 (2013); *Phys. Rev. Lett.* **111**, 257201 (2013).
- [46] Long cylinders are 6×30 or 6×36 sites and shorter cylinders with fixed parameters are 6×12 and 6×20 sites. We keep up to $M = 1600$ or 2000 states depending on the complexity of the Hamiltonian.
- [47] For $\Delta = 0.76$, $J_{\pm\pm} = 0.26J$, $J_{z\pm} = 0.45J$ ($J_{\pm} = 0.66J_z$, $J_{\pm\pm} = 0.34J_z$, $J_{z\pm} = 0.6J_z$ in the notations of Ref. [13]), ordered moment is $\langle S \rangle \approx 0.4694(0.4763)$ by DMRG (SWT).
- [48] $\mathcal{S}(\mathbf{q}) = \sum_{\alpha\beta} (\delta_{\alpha\beta} - q_{\alpha}q_{\beta}/q^2) \mathcal{S}_{\mathbf{q}}^{\alpha\beta}$ is obtained from the spin-spin correlation function $\mathcal{S}_{\mathbf{q}}^{\alpha\beta} = \sum_{i,j} \langle S_i^{\alpha} S_j^{\beta} \rangle e^{i\mathbf{q}(\mathbf{R}_i - \mathbf{R}_j)}$.
- [49] No significant variation is detected vs q_z .
- [50] $\mathcal{S}(\mathbf{q})$ intensity maps in Fig. 5(c) are nearly identical, with the largest discrepancy $< 5\%$ in the entire Brillouin zone. Individual real-space $\langle S_i^{\alpha} S_j^{\beta} \rangle$ correlations with distances $|r_{ij}|$ up to $6a$ are also nearly identical [43].

Topography of Spin Liquids on a Triangular Lattice: Supplemental Material

Zhenyue Zhu,¹ P. A. Maksimov,¹ Steven R. White,¹ and A. L. Chernyshev¹

¹*Department of Physics and Astronomy, University of California, Irvine, California 92697, USA*

(Dated: February 9, 2018)

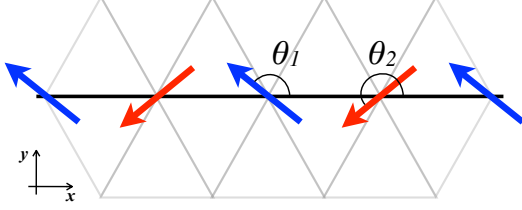


FIG. 1: An example of a counter-rotating spins configuration that minimizes classical energy of the $J_{\pm\pm} < 0$ term along the x -axis bond with $\theta_2 = -\theta_1 \pmod{2\pi}$.

Model and classical phase diagram

Model.—The nearest-neighbor model on an ideal triangular lattice with spin anisotropies constrained by the lattice symmetries [1] can be written as a sum of the conventional XXZ and bond-dependent terms,

$$\mathcal{H} = \mathcal{H}_{XXZ} + \mathcal{H}_{\pm\pm} + \mathcal{H}_{z\pm},$$

$$\mathcal{H}_{XXZ} = J_1 \sum_{\langle ij \rangle} (S_i^x S_j^x + S_i^y S_j^y + \Delta S_i^z S_j^z), \quad (1)$$

$$\mathcal{H}_{\pm\pm} = 2J_{\pm\pm} \sum_{\langle ij \rangle} (\cos \tilde{\varphi}_\alpha (S_i^x S_j^x - S_i^y S_j^y) - \sin \tilde{\varphi}_\alpha (S_i^x S_j^y + S_i^y S_j^x)), \quad (2)$$

$$\mathcal{H}_{z\pm} = J_{z\pm} \sum_{\langle ij \rangle} (\cos \tilde{\varphi}_\alpha (S_i^y S_j^z + S_i^z S_j^y) - \sin \tilde{\varphi}_\alpha (S_i^x S_j^z + S_i^z S_j^x)),$$

where the XXZ anisotropy is taken $0 \leq \Delta \leq 1$ (typical for layered systems), and the “120° phase factors” of the triangular-lattice bond directions along the primitive vectors δ_α in Fig. 1 are $\tilde{\varphi}_\alpha = \{0, -2\pi/3, 2\pi/3\}$.

We note that we use a standard form of the XXZ term in (1) (cf. [1–3] and other works). To relate to the notations of these other works, our $J_1 = 2J_\pm$ and anisotropy $\Delta = J_z/2J_\pm$. These works also use $J_z = \Delta J_1$ as a unity, while we use a more natural J_1 in that role. Although our anisotropic (bond-dependent) terms are the same as elsewhere, we use a different operator form of them in (2) that is significantly more transparent as to what states these terms may be favoring.

Classical states.—For the antiferromagnetic sign of J_1 and $\Delta \leq 1$, the XXZ term (1) favors the well-known 120° state with a plane that is coplanar with the plane of the lattice. It favors a ferromagnetic state if $J_1 < 0$.

The bond-dependent terms in (2) have conflicting

trends along different bond directions. Consider the $J_{\pm\pm}$ term along δ_1 (x -axis bond, $\tilde{\varphi}_1 = 0$). Taking this bond direction in isolation, i.e., along the x -axis 1D chain, this term is given by $2J_{\pm\pm} \sum_{\langle ij \rangle} (S_i^x S_j^x - S_i^y S_j^y)$. As one can see from a transformation $S_i^y \rightarrow -S_i^y$ at every second site of the chain, this term preserves a $U(1)$ symmetry in the x - y plane (plane of the lattice). The classical set of states that is favored by such a term is a two-sublattice configuration of counter-rotating spins, which minimizes $J_{\pm\pm} \cos(\theta_1 + \theta_2)$ at every bond, here θ_1 and θ_2 are the in-plane angles of spins in the two sublattices, respectively. Thus, $\theta_2 = \pi - \theta_1$ for $J_{\pm\pm} > 0$ and $\theta_2 = -\theta_1$ for $J_{\pm\pm} < 0$; see Fig. 1. This is not unlike the trend observed in the “striphyhoneycomb” γ -Li₂IrO₃ [4], another material with strong spin-orbit-generated spin anisotropies where the counter-rotating spiral ordering has been observed and linked to the large Kitaev terms.

The situation is similar for the $J_{z\pm}$ term along the x -axis bond, except that the plane of the counter-rotation of spins is y - z , i.e., spins are perpendicular to the optimized bond and are not contained to the plane of the lattice. The angle of the counter-rotation is also different, as it is minimizing $J_{z\pm} \sin(\theta_1 + \theta_2)$, so $\theta_2 = \pm\pi/2 - \theta_1$.

It is clear, however, that these 1D trends along different bond directions are in conflict with each other. Consideration of the $J_{\pm\pm}$ term along the other bond directions δ_α gives the energy minimized by different angles of counter-rotation: $\theta_2 = \pi - \theta_1 - \tilde{\varphi}_\alpha$ for $J_{\pm\pm} > 0$ and $\theta_2 = -\theta_1 - \tilde{\varphi}_\alpha$ for $J_{\pm\pm} < 0$. For the $J_{z\pm}$ term, the planes of spin counter-rotation are perpendicular to the corresponding bonds. That is, the angles (or planes in the $J_{z\pm}$ case) of the counter-rotated spins depend on the bond direction itself. Also, the triangular-lattice geometry is frustrating for the two-sublattice arrangements.

Therefore, even in the absence of the other competing terms, because of the conflicting preferences on different bonds of the lattice, $J_{\pm\pm}$ and $J_{z\pm}$ interactions break continuous symmetries. We would like to stress that this mechanism of symmetry breaking is different from that of, e.g., Ising-like anisotropies, which explicitly break spin rotational symmetry on any bond.

As a result, only a discrete set of states can be favored by $J_{\pm\pm}$ and $J_{z\pm}$ as the classical ground states, and collinear (“stripe”) phases of two types, referred to as “stripe- \mathbf{x} ” and “stripe- \mathbf{yz} ”, are selected as such; see Fig. 2 and also Refs. [2, 3]. Thus, at the first glance, the above consideration of the counter-rotated spin configurations is completely irrelevant. However, this is not

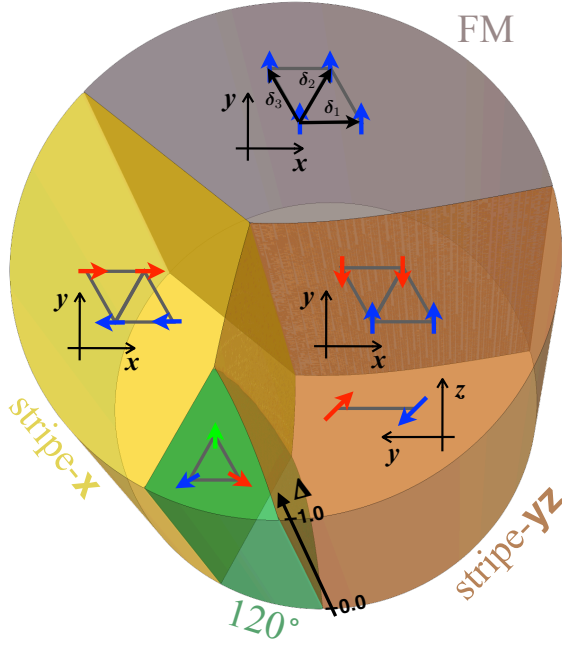


FIG. 2: The 3D classical phase diagram of the model (1), (2) represented using cylindrical parametrization of the parameters (see the text). Sketches of the phases together with primitive vectors of the lattice are shown and phases are discussed in the text in detail. See Fig. 1 of the main text for a 2D cut of this phase diagram at $\Delta=1.0$ in more details.

so, as, in fact, it explains why stripes, and the stripes of these particular types, are selected.

Stripe states.—Consider the “stripe- \mathbf{x} ” state, favored by the $J_{\pm\pm} < 0$ and unaffected by the $J_{z\pm}$ term. Spins co-align with the x -axis bond and with each other along the same bond direction in a ferromagnetic chain structure (“stripe”). The ferromagnetic direction of the stripe alternates from one x -row to the other; see Fig. 2. Needless to say, the ferromagnetic arrangements co-aligned with the x -bond are the two out of four collinear states from the counter-rotating manifold of states favored by $J_{\pm\pm} < 0$ as far as the x -direction is concerned, $\theta_2 = -\theta_1 = \pi$ and $\theta_2 = -\theta_1 = 0$; see Fig. 1. Therefore, classically, the $J_{\pm\pm}$ term is fully satisfied on the x -bond for the “stripe- \mathbf{x} ” arrangement and the other two bonds are half-satisfied and, thus, are only partially frustrated [5]. The other two collinear states are antiferromagnetic x -chains with the moments normal to the x -bond, $\theta_2 = -\theta_1 = \pm\pi/2$. They are more frustrated and are higher in energy.

In a sense, the resultant stripe phases are a result of locking together of the counter-rotating preferences of the bond-dependent terms for different directions in a partially-frustrated fashion.

For the $J_{\pm\pm} > 0$ term, selection of the “stripe- \mathbf{yz} ” state is identical to the one above with the only difference that the ferromagnetic moments now point perpendicular to the x -bond, along the y -axis, $\theta_2 = \pi - \theta_1 = \pi/2$, but are still in the plane of the lattice.

The $J_{z\pm}$ term also favors the ferromagnetic x -chain with spins normal to the x -bond, but with a tilt out of plane toward the z -axis, hence the name “stripe- \mathbf{yz} ”. The direction of ferromagnetic moment of stripes alternates from one x -row to the other; see Fig. 2 and Ref. [3]. If only the $J_{z\pm}$ term is present, the tilt angle is $\pi/4$. When both $J_{\pm\pm} > 0$ and $J_{z\pm}$ terms are present, they both benefit from the “stripe- \mathbf{yz} ” order with x -bond fully satisfied and the tilt angle interpolating between 0 and $\pi/4$ depending on the ratio $J_{z\pm}/J_{\pm\pm}$.

Classical phase diagram.—In Fig. 1, we present the classical 3D phase diagram of the nearest-neighbor triangular-lattice model (1), (2) with all four phases discussed above. Fig. 1 of the main text contains its $\Delta=1.0$ cut. We have used the cylindrical parametrization of the parameter space with the vertical axis mapped on $0 \leq \Delta \leq 1$, $J_{z\pm}$ as the radial, and J_1 and $J_{\pm\pm}$ as the polar variables, so that each horizontal cut represents the entire two-dimensional space of the model at fixed Δ :

$$(J_1, 2J_{\pm\pm}, 5J_{z\pm}) = \left(-r \sin \varphi, r \cos \varphi, \sqrt{1-r^2} \right), \quad (3)$$

such that $\sqrt{J_1^2 + (2J_{\pm\pm})^2 + (5J_{z\pm})^2} = 1$. The particular choice of numerical coefficients in this parametrization is to greatly exaggerate the region where all parameters are of the same order $J_{\pm\pm}, J_{z\pm} \lesssim J_1$.

One can see that the only noticeable change vs Δ from the XY ($\Delta=0$) to the Heisenberg ($\Delta=1.0$) limit of the XXZ part of the model is a slight narrowing of the 120° phase in the $J_{z\pm}$ direction. The boundaries between all the phases shown in Fig. 1 can be found analytically [3]. We reproduce them here with the additional boundaries for the ferromagnetic region:

$$\begin{aligned} \text{s-}\mathbf{x} - 120^\circ &: \quad \eta = -\frac{1}{8}, \\ \text{s-}\mathbf{yz} - 120^\circ &: \quad \zeta = \sqrt{\left(\frac{1}{8} - \eta\right) \left(\frac{3}{2} - \Delta\right)}, \\ \text{s-}\mathbf{x} - \text{s-}\mathbf{yz} &: \quad \zeta = \sqrt{-2\eta(1 - \Delta - 4\eta)}, \\ \text{s-}\mathbf{x} - \text{FM} &: \quad \eta = 1 \quad (J_1, J_{\pm\pm} < 0), \\ \text{s-}\mathbf{yz} - \text{FM} &: \quad \zeta = \sqrt{(3 + \Delta)(1 + \eta)} \quad (J_1 < 0), \end{aligned} \quad (4)$$

where the first column indicates the phases on the two sides of the transition line and the second the equation for that line. Dimensionless parameters are $\eta = J_{\pm\pm}/J_1$ and $\zeta = J_{z\pm}/J_1$ and abbreviations “s- \mathbf{x} ” and “s- \mathbf{yz} ” for the “stripe- \mathbf{x} ” and “stripe- \mathbf{yz} ” were used.

We note that more complicated, multi- \mathbf{Q} ordered states were suggested to occur near the 120° phase boundaries [2]. We have also observed indications of them in instabilities of magnon branches at incommensurate wavevectors in our spin-wave calculations [5]. Since corresponding regions appear to be very narrow, we do not elaborate on them any further.

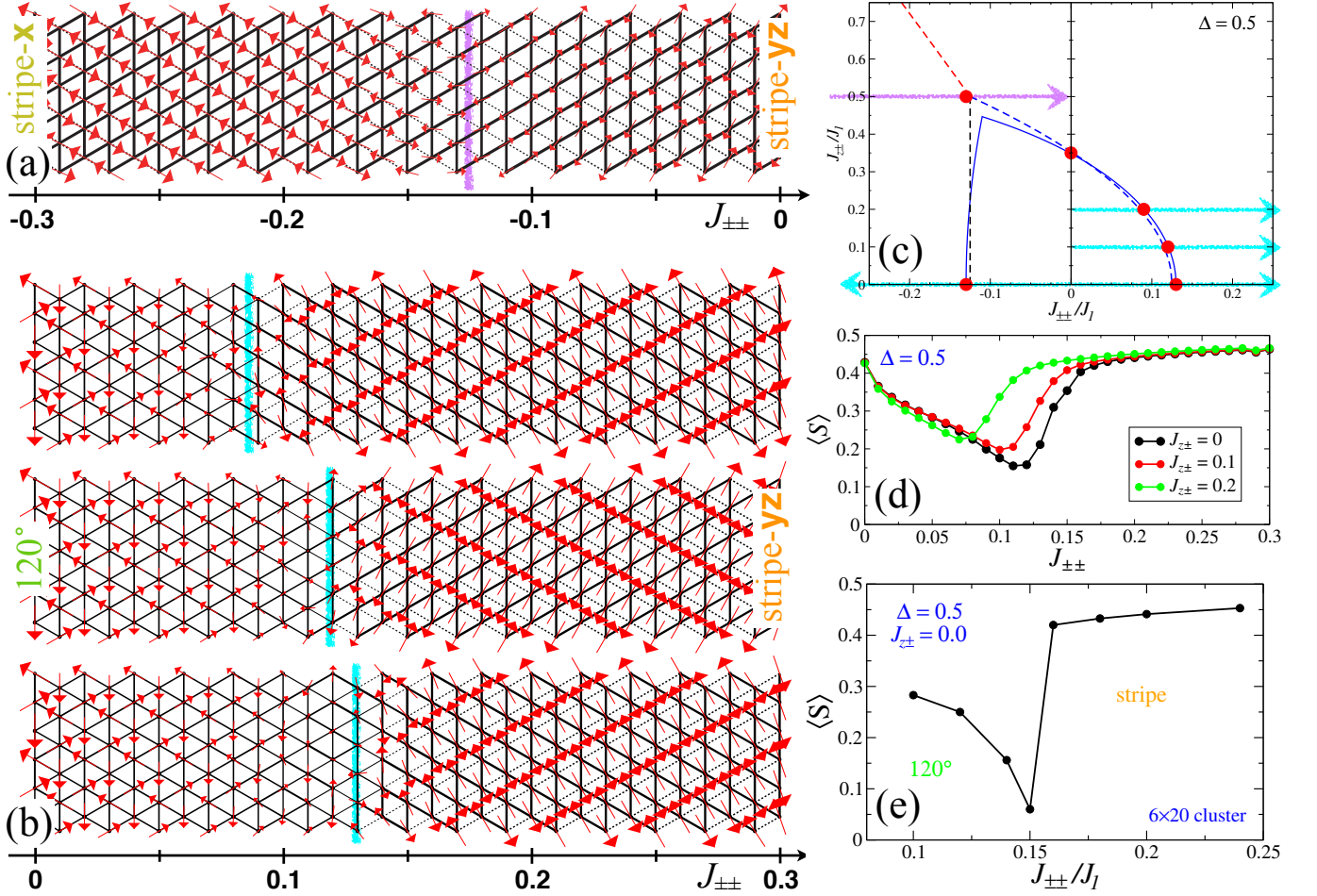


FIG. 3: Results of the 1D long-cylinder DMRG scans for $\langle S \rangle$ vs $J_{\pm\pm}$ for various $J_{z\pm}$ and $\Delta=0.5$. (a) and (b) The real-space images of cylinders with arrows representing the in-plane $\langle S \rangle_{xy}$; vertical lines are inferred transition points. (c) The directions of the cuts, transition points (circles), and classical (dashed lines) and quantum (solid lines) transition boundaries. (d) $\langle S \rangle$ vs $J_{\pm\pm}$ profiles for (b). (e) Is the same using fixed parameter, 6×20 cylinders, for $J_{z\pm}=0.0$ cut vs $J_{\pm\pm}$.

Details of the DMRG calculations

For the DMRG calculations in the 6×30 and 6×36 cylinders, we perform 20 sweeps and typically keep up to $m = 1600$ states with truncation error less than 10^{-5} and in some cases up to $m = 2000$ states and 24 sweeps depending on the complexity of the Hamiltonian. For the 6×12 and 6×20 cylinders, we typically perform 24 sweeps and keep up to $m = 2000$ states with truncation errors less than 10^{-6} . In the real-space images of cylinders, the size of the arrows represent the measurement of the projection of local spin in the xy plane. The width of the bond on the lattice represents the nearest-neighbor spin-spin correlation, with ferromagnetic correlation shown as dashed and antiferromagnetic ones as solid lines.

Phase diagram, $\Delta=0.5$.—In Figs. 3 and 4 we provide a detailed summary of all our DMRG data for $\Delta=0.5$. In Figs. 3(a) and (b), we show the real-space images of the long-cylinder DMRG “scans” along the cuts indicated in Fig. 3(c), all varying $J_{\pm\pm}$ along their length and having

all other parameters fixed. $J_{z\pm}$ is 0.5 for Fig. 3(a) scan and is 0.2, 0.1, and 0.0, top to bottom, in Fig. 3(b), all in units of J_1 (1). The largest arrow in the cylinder images corresponds to the expectation value of the in-plane $\langle S \rangle_{xy} \approx 0.43$ to 0.46. The results at $J_{z\pm} = 0.0$ are symmetric with respect to $J_{\pm\pm} \rightarrow -J_{\pm\pm}$ and “stripe- \mathbf{yz} ” \rightarrow “stripe- \mathbf{x} ”, as indicated in Fig. 3(c).

The scan in Fig. 3(a) shows a direct transition between the “stripe- \mathbf{x} ” state with spins along the bonds and the “stripe- \mathbf{yz} ” state with spins perpendicular to the bond and tilted away from the xy plane. The scans in Fig. 3(b) show a direct transition between the 120° state and the “stripe- \mathbf{yz} ” state. Profiles of $\langle S \rangle$ vs $J_{\pm\pm}$ in Fig. 3(d) from these long-cylinder scans show no indication of a magnetically disordered state. Fig. 3(e) provides a point-by-point “scan” of the phase diagram using 6×20 cylinders with fixed parameters for $J_{z\pm} = 0.0$ vs $J_{\pm\pm}$ in a range 0.1 to 0.24; here $\langle S \rangle$ is measured at the center of such cylinders. These results also suggest a direct transition between the 120° and “stripe- \mathbf{yz} ” states.

In Fig. 4(a), we show the long-cylinder scan along the

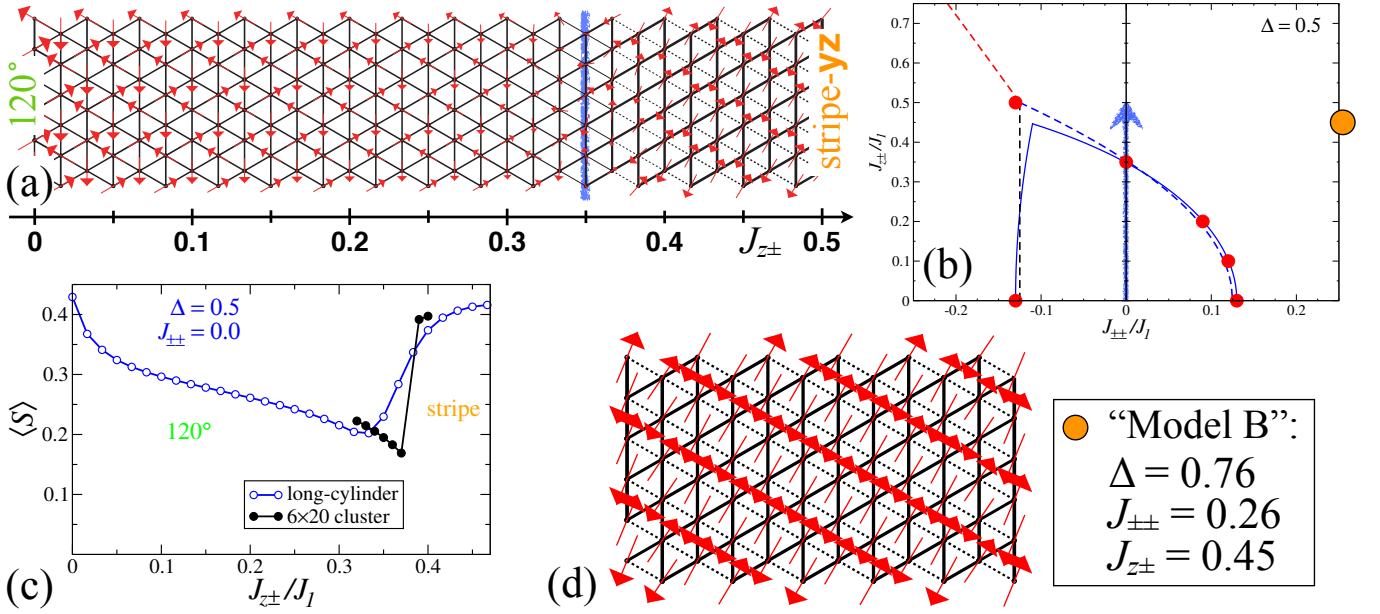


FIG. 4: (a) Same as in Fig. 3(a) and (b) along the $J_{z\pm}$ -axis as shown in (b). (c) The $\langle S \rangle$ vs $J_{z\pm}$ profiles from (a) and from 6×20 cylinders. (d) The ground state for the “Model B” parameters (shown and indicated in (b) by the orange circle) in 6×12 DMRG cylinder. The ordered moment is $\langle S \rangle \approx 0.4694$.

$J_{z\pm}$ -axis at $J_{\pm\pm} = 0$, indicated in Fig. 4(b). It also demonstrates a clear direct transition between the 120° and “stripe- \mathbf{yz} ” states. Fig. 4(c) combines $\langle S \rangle$ vs $J_{z\pm}$ profiles from this scan with the one from 6×20 cylinders with fixed parameters, both unequivocally ruling out potential intermediate states.

Large anisotropies.—We also make a brief note on the case of large anisotropic interactions in (2).

First is the case of a parameter choice that was advocated in Ref. [6] as the prime candidate for a spin-liquid (SL) state and was subsequently used in Ref. [7] with the same attitude. Following [7], we refer to this set of parameters as the “Model B”: $\Delta = 0.76$, $J_{\pm\pm} = 0.26J$, $J_{z\pm} = 0.45J$ ($J_{\pm} = 0.66J_z$, $J_{\pm\pm} = 0.34J_z$, $J_{z\pm} = 0.6J_z$ in the notations of Refs. [6, 7]). The justification of this choice was from the classical, high-temperature simulation, referred to as the self-consistent Gaussian approximation, of the static structure factor, $\mathcal{S}(\mathbf{q})$, yielding results that were seemingly in agreement with the experimental data. While such an agreement is spurious because of an inconspicuous omission of the off-diagonal components of $\mathcal{S}(\mathbf{q})$ in the calculations [8], we provide here the DMRG results for Model B. Although the XXZ anisotropy is somewhat higher than in Fig. 4(b), we indicate the Model B $J_{\pm\pm} - J_{z\pm}$ coordinates by an orange circle. It is clearly deep in the stripe- \mathbf{yz} state, which is confirmed by the DMRG calculation in 6×12 cylinder shown in Fig. 4(d). The ordered moment is $\langle S \rangle \approx 0.4694$, which is also confirmed by spin-wave theory (SWT) calculations that yield $\langle S \rangle \approx 0.4763$. Both results indicate strongly suppressed quantum fluctuations due to anisotropic terms.

Second case are the large values of $J_{z\pm}$. We choose

$\Delta = 1.0$ and $J_{\pm\pm} = 0$ for simplicity. We have tested several $J_{z\pm} = 4.0, 8.0$, and ∞ . DMRG yields the ground states that are virtually identical to the one in Fig. 4(d), i.e., they are all nearly classical stripe- \mathbf{yz} states, with the out-of plane tilt angle changing as a function of $J_{z\pm}$ and reaching $\pi/4$ at $J_{z\pm} = \infty$, in agreement with the classical discussion above. There is a slightly curious observation concerning the behavior of the almost classical ordered moments. The fluctuations are slightly higher at $J_{z\pm} = \infty$ than at intermediate values $J_{z\pm}$, the behavior also replicated by the SWT: $\langle S \rangle \approx 0.4886(0.4914)$ [$J_{z\pm} = 4.0$], $\langle S \rangle \approx 0.4857(0.4903)$ [$J_{z\pm} = 8.0$], and $\langle S \rangle \approx 0.4795(0.4869)$ [$J_{z\pm} = \infty$] by DMRG (SWT).

No indication of a massive degeneracy due to large anisotropic interactions has been identified.

Phase diagram, $\Delta = 1.0$.—Our summary of the DMRG data for $\Delta = 1.0$ in Figs. 5 and 6 is structured similarly to the one for $\Delta = 0.5$ above. The directions of the long-cylinder DMRG scans for Figs. 5(a) and (b) are indicated in Fig. 5(c). As before, the transition at a large $J_{z\pm} = 0.5$ in Fig. 5(a) is a direct one between the stripe- \mathbf{x} and the stripe- \mathbf{yz} states and Fig. 6(f) demonstrates that by the profile of $\langle S \rangle$ throughout this transition. Although this is harder to appreciate visually in the real-space images of cylinders in Fig. 5(b), they still show direct transitions between the 120° and the stripe- \mathbf{yz} state for $J_{z\pm} = 0.2, 0.1$, and 0.0 , with the profiles of $\langle S \rangle$ vs $J_{\pm\pm}$ from these long-cylinder scans shown in Fig. 5(d). This is verified by the 6×20 cylinders “scan” with fixed parameters for $J_{z\pm} = 0.0$ in Fig. 5(e). Although the 120° order parameter is reduced, this analysis also supports a direct transition without an intermediate state.

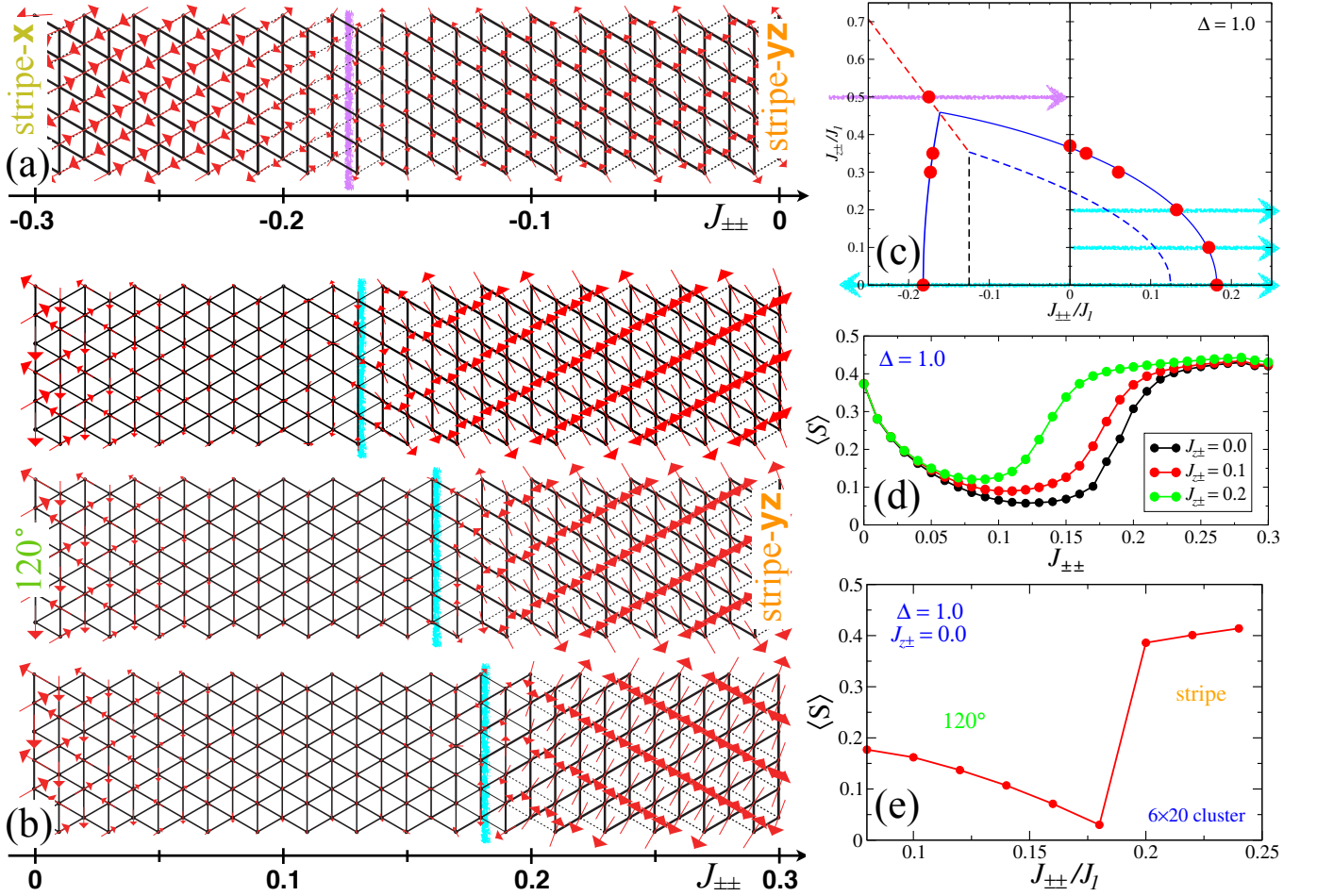


FIG. 5: Results of the 1D long-cylinder DMRG scans for $\langle S \rangle$ vs $J_{\pm\pm}$ for various $J_{z\pm}$ and $\Delta = 1.0$. (a) and (b) The real-space images of cylinders with arrows representing the in-plane $\langle S \rangle_{xy}$; vertical lines are inferred transition points. (c) The directions of the cuts, transition points (circles), and classical (dashed lines) and quantum (solid lines) transition boundaries. (d) $\langle S \rangle$ vs $J_{\pm\pm}$ profiles for (b). (e) Is the same using fixed parameter, 6×20 cylinders, for $J_{z\pm} = 0.0$ cut vs $J_{\pm\pm}$.

Another observation from these data is that the 120° state has expanded beyond its classical phase boundaries at the cost of the stripe states, as discussed in the main text. This can be expected as the excitations in the 120° state remain gapless despite anisotropic terms and, therefore, allow for more quantum fluctuations to lower its energy as opposed to the stripe phases that are all gapped.

In Figs. 6(a) and (b) we show the long-cylinder scans along the $J_{z\pm}$ -axis at $J_{\pm\pm} = 0$ and two additional scans that are parallel to the $J_{\pm\pm}$ -axis at $J_{z\pm} = 0.3$ and 0.35 , respectively, with the cuts indicated in Fig. 6(b). At the first glance, the $\langle S \rangle$ vs $J_{z\pm}$ profile from the scan in Fig. 6(a) is not too different from, e.g., one of the profiles in Fig. 5(d). On a closer inspection that uses a smaller range of $J_{z\pm}$ and thus a smaller gradient of $J_{z\pm}$, one can observe an indication of the magnetically disordered (SL) state between the 120° and the stripe-yz states; see Fig. 6(d). The same Fig. 6(d) shows the results of the 6×20 cylinders “scan” of the same area with fixed parameters. It shows a distinct “kink” in $\langle S \rangle$ at about $J_{z\pm} \approx 0.28$, indicative of a transition. One can

see, however, that the intermediate phase from $J_{z\pm} \approx 0.28$ to 0.38 still exhibits a weak order. This, combined with the $1/L$ -scaling analysis below may suggest that a weak and/or a more complicated form of ordering referred to as the multi- \mathbf{Q} states [2] cannot be fully ruled out for that region. We, therefore, mark it as a “suspected” spin-liquid, or “SL ?” region.

The two other long-cylinder DMRG scans in Fig. 6(b) span the range of $J_{\pm\pm}$ that connects the two stripe phases. The profiles of $\langle S \rangle$ vs $J_{\pm\pm}$ from these scans shown in Fig. 6(e) show a clear trend to a much suppressed order between the two stripe phases, which is clearly distinct from the scans for the smaller $J_{z\pm}$ and for $\Delta = 0.5$ case. Fig. 6(e) indicates that the suspected SL region covers the entire area between the stripe-x and stripe-yz phases above $J_{z\pm} \approx 0.28$ and up to the tricritical point at $[J_{\pm\pm} \approx -0.17, J_{z\pm} \approx 0.45]$.

Phase diagram, $\Delta = 0.8$.—We continue investigation of the model (1), (2) in the plane of $\Delta = 0.8$ with scans similar to the ones in Figs. 6(b) and (d). Our Fig. 7(a) presents the real-space images of the long-cylinder scans

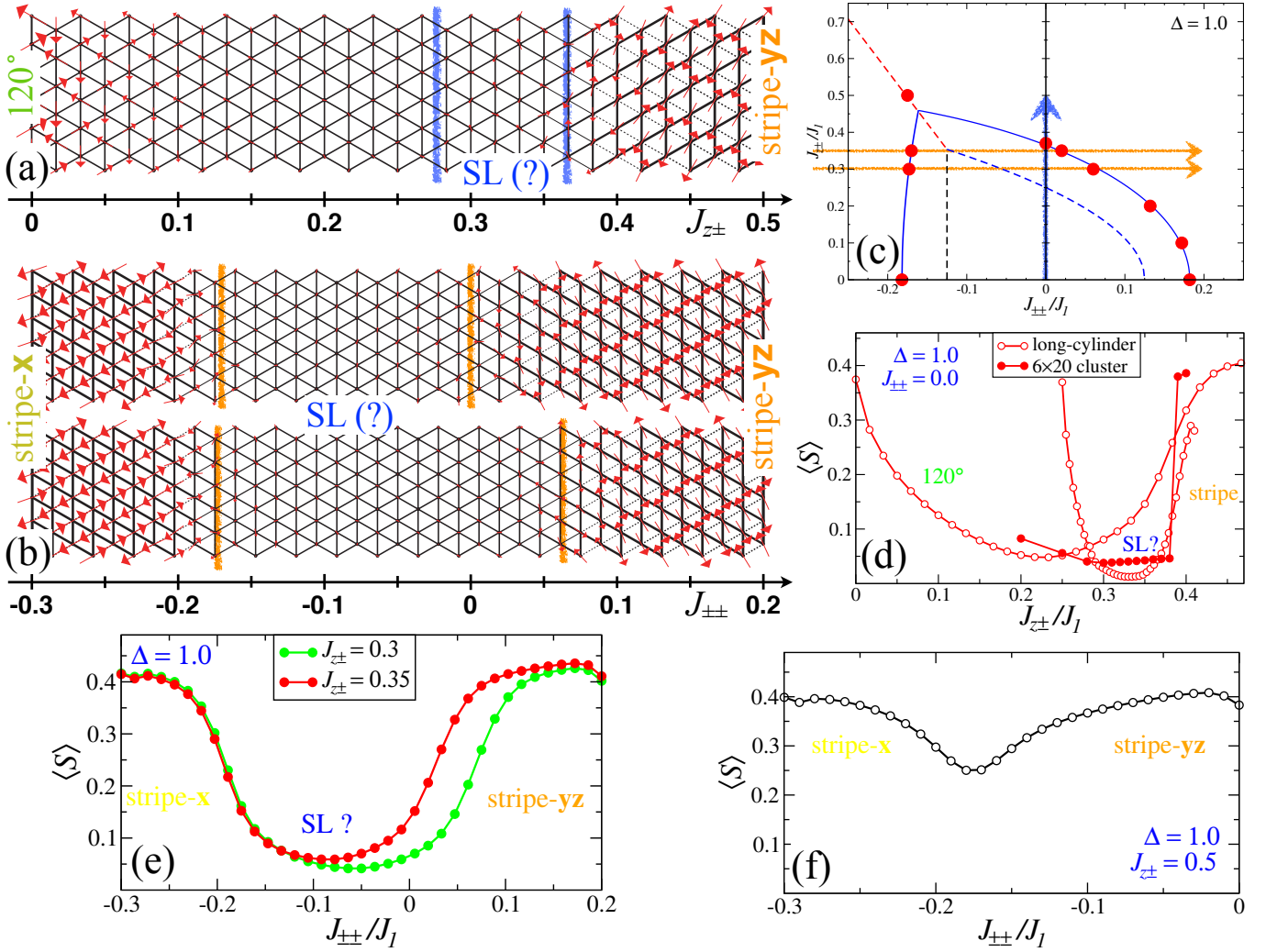


FIG. 6: (a) and (b) Same as in Fig. 5(a) and (b) along the $J_{z\pm}$ -axis and parallel to the $J_{\pm\pm}$ -axis at $J_{z\pm} = 0.3$ and 0.35 as is shown in (c). (d) The $\langle S \rangle$ vs $J_{z\pm}$ profiles from (a), a long cylinder with smaller $J_{z\pm}$ range, and from 6×20 cylinders. (e) The $\langle S \rangle$ vs $J_{\pm\pm}$ profiles from the scans in (b). (f) The $\langle S \rangle$ vs $J_{\pm\pm}$ profile from the scan in Fig. 5(a).

along the cuts parallel to the $J_{\pm\pm}$ -axis at $J_{z\pm} = 0.3$ and 0.35 , indicated in Fig. 7(b), same as in Fig. 6. Fig. 7(c) shows $\langle S \rangle$ vs $J_{\pm\pm}$ profiles for these cuts and Fig. 7(d) shows the scan by the 6×20 cylinders with fixed parameters along the $J_{z\pm}$ -axis at $J_{\pm\pm} = 0$ for the region near transition to the stripe phase.

It is useful to compare with the results for $\Delta = 1.0$ in Fig. 6. First, the expansion of the 120° state beyond the classical phase boundaries is still present, but is significantly smaller; see Fig. 7(b). Second, the $J_{z\pm} = 0.3$ cut in Figs. 7(a) and (c) shows that the 120° state reclaims its territory from the spin-liquid state. Note that there are no boundary conditions applied at the ends of long cylinders where a stripe state is expected, so the appearance of the 120° state in the middle of the $J_{z\pm} = 0.3$ scan is entirely spontaneous. The $J_{z\pm} = 0.35$ cut shows an intermediate SL state between the two stripe phases as before, but in a narrower region. Lastly, the fixed-

parameter, smaller cylinder scan in Fig. 7(d) still shows a kink-like feature and a flat $\langle S \rangle$ in the narrow intermediate phase from $J_{z\pm} \approx 0.35$ to 0.38 , also suggesting a much shrunk “suspected SL” state.

One can see that the suspected SL region clearly retreats as Δ is reduced from the isotropic limit of the bond-independent, XXZ part of the model (1). The extrapolations of the boundaries of the SL region indicate that it disappears completely at about $\Delta \approx 0.7$.

Phase diagram, scan vs Δ .—The last statement is verified by an additional 1D DMRG scan from the middle of the suspected SL region in the $\Delta = 1.0$ plane at $J_{\pm\pm} = -0.075$ and $J_{z\pm} = 0.35$ (marked by a turquoise star in Fig. 2 of the main text) along the Δ -axis toward a well-formed 120° region at $\Delta = 0.5$. The results are shown in Fig. 8(a) and (b). The boundary on the SL side is open (no boundary conditions) with one site removed to avoid spinon localization, common to Z_2 spin-liquid states [9].

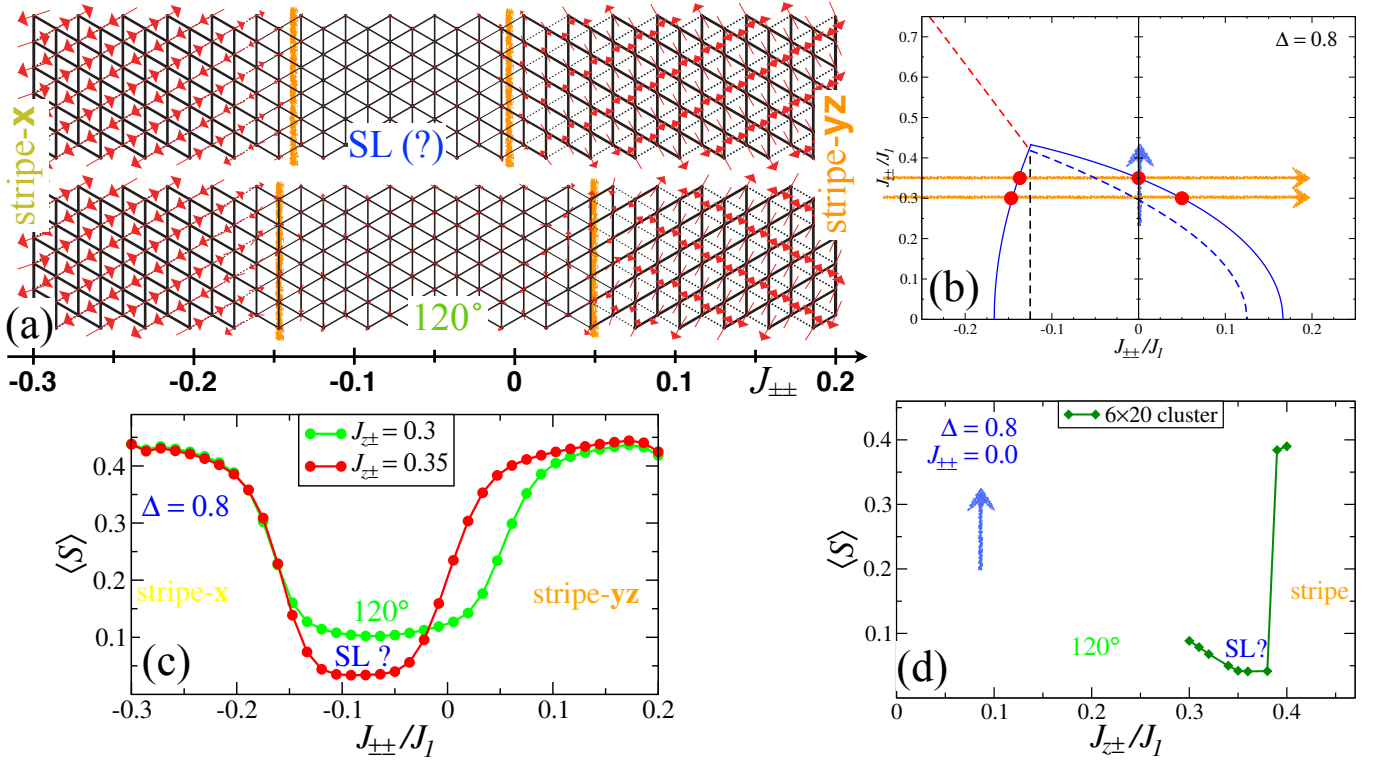


FIG. 7: Same as in Fig. 6 for $\Delta = 0.8$. (a) The scans parallel to the $J_{\pm\pm}$ -axis at $J_{\pm\pm} = 0.3$ and 0.35 as is shown in (b) [c.f. Fig. 6(b)]. (c) The $\langle S \rangle$ vs $J_{\pm\pm}$ profiles from the scans in (a) [c.f. Fig. 6(e)]. (d) The $\langle S \rangle$ vs $J_{\pm\pm}$ profile from 6×20 cylinders for the cut along the $J_{\pm\pm}$ -axis [c.f. Fig. 6(d)].

The 120° order parameter profile shows a transition to a magnetically disordered state at $\Delta \gtrsim 0.7 \pm 0.05$, confirming our estimate from the extrapolation above. In the long-cylinder profile of $\langle S \rangle$, there is an additional kink at $\Delta \gtrsim 0.62$, suggestive of an intermediate ordered state.

1/L extrapolations.—Yet another test of the SL region is provided by the $1/L$ scaling of the order parameter $\langle S \rangle$, measured at the center of the cluster, using a sequence of clusters with the fixed aspect ratio [10]. In Figs. 8(c) and (d), we reproduce for clarity two of such $1/L$ extrapolations from Fig. 3 of the main text. They show $\langle S \rangle$ vs $1/L_y$ using clusters 3×6 and 6×12 for two sets of $J_{\pm\pm}$ and $J_{z\pm}$ from the suspected SL region for $\Delta = 1.0$ and also for smaller $\Delta = 0.8$ and 0.5 . The extrapolated values of the order parameter $\langle S \rangle_\infty$ are shown on the vertical axes of Figs. 8(c) and (d) and plotted in their insets as a function of Δ . This analysis indicates that the SL region of the 3D parameter space is likely much smaller than found by the cylinder scans. For instance, the $1/L$ extrapolation demonstrates a weak order along the $J_{z\pm}$ -axis even for $\Delta = 1.0$, see Fig. 8(c), and the extent of the 3D SL region along the Δ -axis is limited by $\Delta \approx 0.9$, see Figs. 8(d), not by $\Delta \lesssim 0.7$ as was found earlier.

This dichotomy of the results from the complementary methods must be contrasted with the case of the other well-studied spin-liquids, such as the isotropic J_1 –

J_2 model on the triangular lattice [9]. In Fig. 8(e) we demonstrate the $1/L$ scaling for this model using the same set of clusters for several values of J_2 (in units of J_1). The extrapolations and the plot of $\langle S \rangle_\infty$ vs J_2 in the inset show a transition to an SL state at $J_2 \gtrsim 0.06$, the value that is in an almost precise agreement with several other criteria, such as the long-cylinder scans, correlation length decay, and energy extrapolation [5, 9]. This is not the case in the present study, and while the exact reason for such a lack of a close agreement by different methods is unclear, we suspect that this might be another indication of a remnant or a competing order.

Summary of the nearest-neighbor model.—With the help of the data described above, we are able to construct an approximate phase diagram of the quantum, $S = 1/2$, nearest-neighbor anisotropic triangular-lattice model in (1), (2), see Fig. 4 of the main text, in which we give a generous outline to the spin-liquid state region according to the results of the long-cylinder scans. The SL state forms a deformed cone-like shape in a proximity of the line where all three classical phases, the 120° , the stripe-**x**, and the stripe-**yz** states meet with a limited extent along the Δ -axis and into the classical 120° region. From this analysis it is clear that the suspected SL state has the largest footprint in the $\Delta = 1.0$ plane and is, thus, favored by a more isotropic form of the XXZ

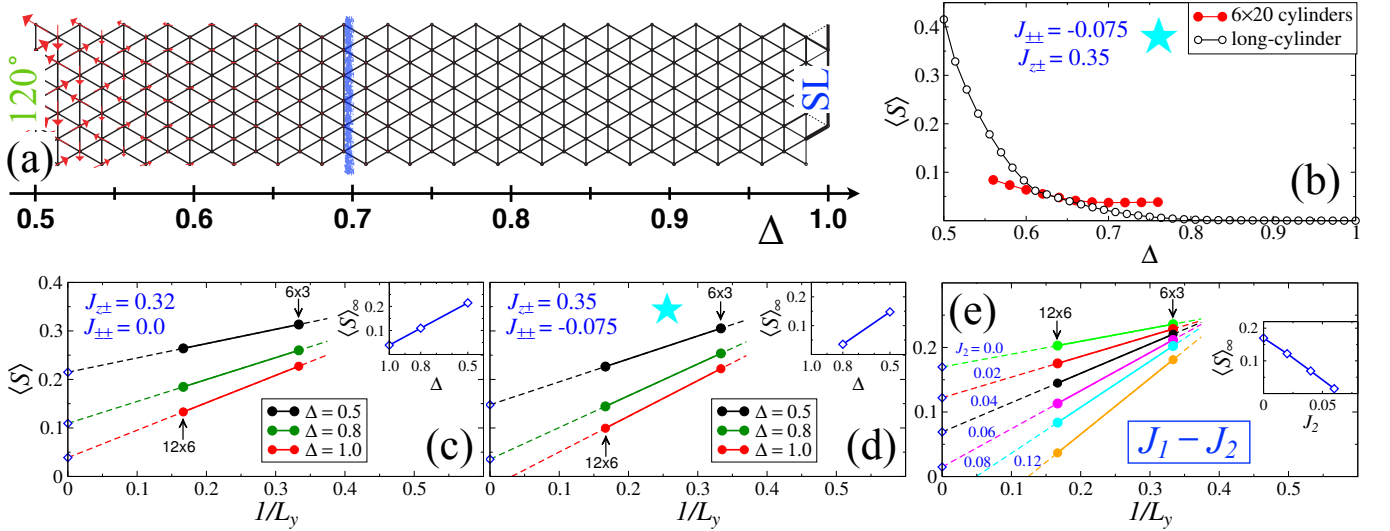


FIG. 8: (a) and (b) The long-cylinder 1D DMRG scan and $\langle S \rangle$ profile at $[J_{\pm\pm}, J_{z\pm}] = [-0.075, 0.35]$ along the Δ -axis, respectively. In (b), results from 6×20 cylinders are also shown. (c) and (d) The $1/L_y$ extrapolation of $\langle S \rangle$ in the nearest-neighbor anisotropic triangular-lattice model (1), (2) for $\Delta = 1.0, 0.8$, and 0.5 and for $[J_{\pm\pm}, J_{z\pm}] = [0.0, 0.32]$ [(c)] and for $[J_{\pm\pm}, J_{z\pm}] = [-0.075, 0.35]$ [(d)]. The insets show extrapolated values $\langle S \rangle_\infty$ vs Δ . (e) The same for the J_1-J_2 model, inset shows extrapolated values of $\langle S \rangle_\infty$ vs J_2 .

part of the model (1), contrary to the expectations that the anisotropic terms in (2) are the ones that are driving the system to a massive degeneracy that generates an SL state. This feature also hints at a possible connection with the other forms of spin-liquid states in an extended phase diagram of the model that we explore next.

J_2 -extension

There are two reasons to be interested in a wider parameter space that extends the nearest-neighbor anisotropic triangular-lattice model of (1), (2). First, the experiments in YbMgGaO_4 (YMGO), one of the most-studied experimental realization of such a model, strongly suggest a sizable second-nearest-neighbor J_2 term [11]. Second, the spin liquid in the isotropic J_1-J_2 model on the triangular lattice is well studied [9], so it would be very informative to establish a relation between the spin liquids in these models, if it exists.

For both reasons, a minimalistic modification of the nearest-neighbor model (1), (2) by the XXZ -only next-nearest-neighbor J_2 -term suffices

$$\mathcal{H}_{XXZ}^{J_2} = J_2 \sum_{\langle\langle ij \rangle\rangle} (S_i^x S_j^x + S_i^y S_j^y + \Delta S_i^z S_j^z), \quad (5)$$

where we also assume that the XXZ anisotropy is the same as in the J_1 -term in (1).

There are several ways of representing the four-dimensional parameter space of the resultant extended model. One is offered in our Fig. 4 of the main text, in which the back panel represents a topographic map of the nearest-neighbor model and the bottom panel is

such a map for the XXZ $J_1-J_2-J_{\pm\pm}$ (or anisotropic J_1-J_2 , $J_{z\pm} = 0$) model, where the topographic axis for both panels is the XXZ anisotropy Δ . For the latter model, we used the results obtained by us previously in Ref. [5]. Such a “dual” map is suggestive of the connectivity between the corresponding 2D “puddles” of the SL states in the two panels via some $J_{z\pm}-J_2$ “tube” for a fixed Δ .

It is also natural to expect such a connection from the purely classical phase diagram. For a fixed Δ , the 3D parameter space is given by the $(J_2, J_{\pm\pm}, J_{z\pm})$ triad and the region occupied by the 120° state is a deformed tetrahedron, with an example of the phase diagram for $\Delta = 1.0$ shown in Fig. 10(a). The back and the bottom panels of it are the same as in Fig. 4 of the main text. Since the SL states in both 2D panels occur in a proximity of a 120° -to-stripe-to-stripe tricritical point, then the connection, if it exists, should be expected along the $J_{z\pm}-J_2$ tricritical rim of the 120° state tetrahedron in Fig. 10(a).

A somewhat different 3D “cut” of the 4D parameter space is offered in Fig. 9(a). Instead of fixing Δ , we select a plane of $J_{\pm\pm} = 0$ in Fig. 10(a) and add Δ as the third axis, with the resultant triad being $(J_{z\pm}, J_2, \Delta)$. Such a choice is motivated by the fact that $J_{\pm\pm}$ is detrimental to the J_1-J_2 spin-liquid state according to our previous study [5]. Thus, the left-hand-side panel in Fig. 9(a) is the $J_{\pm\pm} = 0$ section of the 3D diagram of the nearest-neighbor model and the right-hand-side one is the phase diagram of the XXZ J_1-J_2 model.

The isotropic J_1-J_2 model ($\Delta = 1.0$) has a spin-liquid ground state for a range of J_2 between 0.06 and 0.16 (units of J_1) [9]. As we have shown in our previous study [5], it survives the XXZ anisotropy down to $\Delta \approx 0.3$; see Fig. 9(a). One can see that both

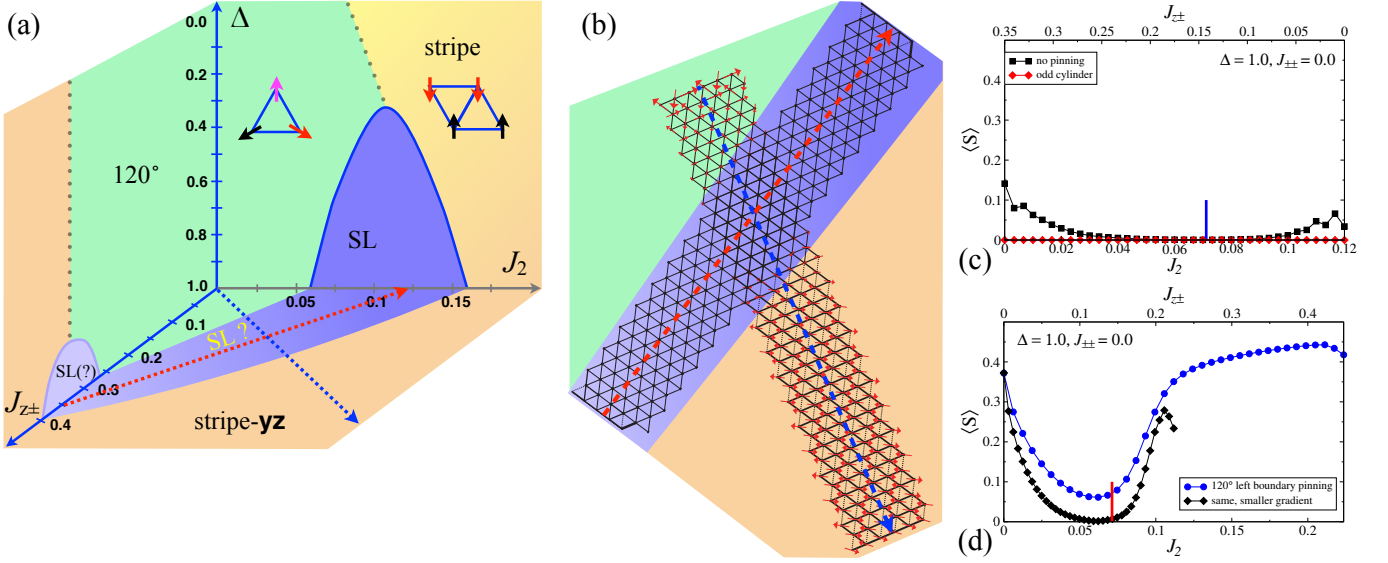


FIG. 9: (a) The 3D, $(J_{z\pm}, J_2, \Delta)$ phase diagram of the extended anisotropic model with J_2 at $J_{z\pm} = 0$. The l.h.s. and r.h.s. panels are the 2D $J_{z\pm} = 0$ section of the 3D diagram of the nearest-neighbor model and the 2D phase diagram of the XXZ J_1 - J_2 model, respectively. Arrows show directions of the 1D long-cylinder DMRG cuts in (b). (b) The real-space images of cylinders with arrows showing directions of the scans and phases marked schematically. (c) and (d) The $\langle S \rangle$ vs J_2 ($J_{z\pm}$) profiles from (b) with different boundary conditions or parameter range, see text. Vertical bars mark the intersection point of the scans.

l.h.s. and r.h.s. panels in Fig. 9(a) have domes of an SL state. A natural test of their compatibility is provided using our 1D DMRG long-cylinder scans shown schematically by arrows in Fig. 9(a), see also Fig. 4 of the main text. For the $(J_{z\pm}, J_2, \Delta)$ coordinates, the scans are along the $(0.35, 0.0, 1.0) \rightarrow (0.0, 0.12, 1.0)$ and $(0.0, 0.0, 1.0) \rightarrow (0.44, 0.22, 1.0)$ directions. The results are presented in Figs. 9(b), (c) and (d), with the vertical bars in Figs. 9(c) and (d) showing the intersection point of the scans, see also Fig. 5(a) and (b) of the main text.

The first of the scans connects anisotropic spin-liquid state identified in Fig. 6 with the isotropic J_1 - J_2 spin liquid known previously [9], from $(J_{z\pm}, J_{z\pm}) = (0.0, 0.35)$ to $J_2 = 0.12$. We have tried two types of boundary conditions as Fig. 9(c) indicates. First is just open boundaries. Second is the same, but with one site removed at each end to suppress spinon localization at the edges [9]. While the first cylinder develops a weak order at the edges, the second scan shows no indication of a magnetic order anywhere along its length, clearly demonstrating that the SLs of the two models are connected. More importantly, this scan displays the same thickness of the bonds along the cylinder, which is proportional to the nearest-neighbor correlation $\langle \mathbf{S}_i \mathbf{S}_j \rangle$, thus showing no change of the character of the SL state anywhere along this scan.

The second scan starts at the Heisenberg, nearest-neighbor point (J_1 -only model) and extends deep into the stripe-yz state. It is complementary to the first scan and is also used to confirm the existence of an intermediate SL state between the 120° and the stripe phases along the direction tilted from both J_2 and $J_{z\pm}$ axes. Fig. 9(d) shows two profiles of $\langle S \rangle$ vs J_2 ($J_{z\pm}$), one for

the entire range of parameters and one for a shorter range and smaller gradient. It clearly demonstrates the robust intermediate SL state, consistent with the first scan as well as with the scans of the same nature along $J_{z\pm}$ and J_2 axes in Fig. 6 and in Ref. [5].

Static structure factor $\mathcal{S}(\mathbf{q})$

While the nearest-neighbor correlator $\langle \mathbf{S}_i \mathbf{S}_j \rangle$ has already demonstrated no change of the character of the SL state anywhere along the long-cylinder scan in Fig. 9, a deeper and more comprehensive insight into the nature of the SL state is offered by the static structure factor, $\mathcal{S}(\mathbf{q}) = \sum_{\alpha\beta} (\delta_{\alpha\beta} - q_\alpha q_\beta / q^2) \mathcal{S}_{\mathbf{q}}^{\alpha\beta}$, a quantity that is also observable in the neutron-scattering experiments. We obtain it from the Fourier transform, $\mathcal{S}_{\mathbf{q}}^{\alpha\beta} = N^{-1} \sum_{ij} \langle S_i^\alpha S_j^\beta \rangle e^{i\mathbf{q}(\mathbf{R}_i - \mathbf{R}_j)}$, of the real-space spin-spin correlation function $\langle S_i^\alpha S_j^\beta \rangle$, where the latter is determined from the ground state wave-function on various DMRG cylinders.

In the main text, we have used correlation function from the different section of the long cylinder in Figs. 9(b),(c), see also Fig. 5 of the main text and its discussion. Here we show $\mathcal{S}(\mathbf{q})$ from the 6×20 cylinders with fixed parameters for three representative sets of data; see Figs. 10(b)-(d). In Figs. 10(b) and (c), $\mathcal{S}(\mathbf{q})$ is for the anisotropic nearest-neighbor model at $\Delta = 1.0$ and for $(J_{z\pm}, J_{z\pm}) = (-0.075, 0.35)$ and $(J_{z\pm}, J_{z\pm}) = (0.0, 0.35)$, respectively. In Fig. 10(d), $\mathcal{S}(\mathbf{q})$ is for the isotropic J_1 - J_2 model at $J_2 = 0.12$. Thus, $\mathcal{S}(\mathbf{q})$ in Figs. 10(c) and (d) correspond to the beginning and the end of the long-

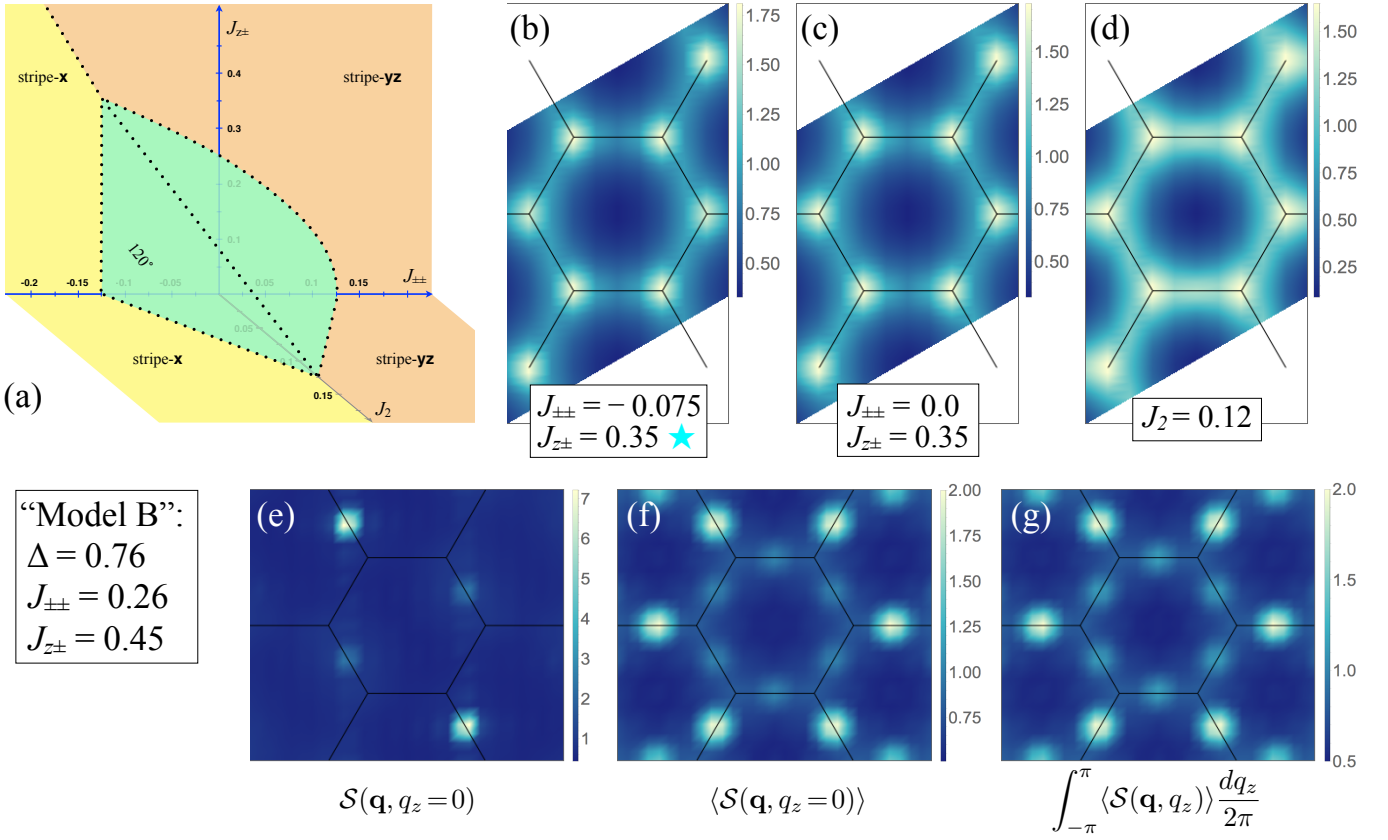


FIG. 10: (a) The classical 3D phase diagram of the J_2 -extended model at $\Delta = 1.0$. (b)-(d) Static structure factor, $\mathcal{S}(\mathbf{q})$, from the 6×20 cylinders for the anisotropic nearest-neighbor model at $\Delta = 1.0$ at $(J_{\pm\pm}, J_{z\pm}) = (-0.075, 0.35)$ [(b)] and $(J_{\pm\pm}, J_{z\pm}) = (0.0, 0.35)$ [(c)], and for the isotropic J_1 - J_2 model at $J_2 = 0.12$ [(d)]. (e)-(g) $\mathcal{S}(\mathbf{q})$ for the stripe state, “Model B” parameters, at $q_z = 0$ [(e)], averaged over three domain orientations [(f)], and integrated over q_z [(g)].

cylinder scan in Fig. 9 marked by the red arrow. The $\mathcal{S}(\mathbf{q})$ in Fig. 10(b) is also from the SL region of the nearest-neighbor anisotropic triangular-lattice model of (1), (2); see Fig. 6, Figs. 2 and 3 of the main text, and Fig. 7, where it is marked by a star symbol.

One can see that while there is some minor variation in intensity and overall scale, the static structure factor is essentially the same for all three parameter sets, confirming the results inferred from the long-cylinder scan. This implies, once more, that the SLs in the anisotropic nearest-neighbor model and in the fully isotropic J_1 - J_2 model, as well as in any interpolating SL state, are isomorphic to each other.

Of the discussed models, the isotropic J_1 - J_2 model is most studied [9], see the main text for a more comprehensive list of references. The exact nature of its spin-liquid state is still under debate, with the broadened peak in $\mathcal{S}(\mathbf{q})$ at the K -points consistent with the nematic Z_2 [9], $U(1)$ Dirac, chiral, and Dirac-like spin-liquids. One thing is clear: it is *not* consistent with the “open spinon Fermi surface” SL state proposed for YMGO [12], see also Ref. [13]. This observation alone is sufficient to suggest that an extrinsic mechanism is responsible for an SL-like response in this material.

Three additional points are in order. In the spin-liquid states in Figs. 10(b)-(d), $\mathcal{S}(\mathbf{q})$ is essentially isotropic, meaning that the contribution of the off-diagonal terms in it, $\mathcal{S}_{\mathbf{q}}^{\alpha\beta}$, are negligible in our results, a feature naturally expected for a magnetically isotropic, spin-liquid-like state. In addition, there is only a very weak q_z dependence of $\mathcal{S}(\mathbf{q})$ and the broadened peaks are obviously the same in different Brillouin zones.

Consider now a stripe state. For clarity, we choose the “Model B” set of parameters discussed in Figs. 4(b) and (d). Our Fig. 10(e) shows $\mathcal{S}(\mathbf{q})$ for it at $q_z = 0$ and Fig. 10(f) shows the same data averaged over three possible stripe orientations. The last Figure 10(g) is the same integrated over q_z . First, experiments in YMGO [11, 12] show the structure factor with the maxima of intensity at the M -points, a feature easily obtainable from a mixture of stripe domains, see Fig. 10(f), supporting a scenario of the disorder-induced spin-liquid mimicry in YMGO, proposed by us in Ref. [5].

In addition, we have verified that: (i) the role of the off-diagonal terms in $\mathcal{S}(\mathbf{q})$ of the stripe phase in Figs. 10(e)-(f) is substantial, (ii) $\mathcal{S}(\mathbf{q})$ has a significant q_z variation, and (iii) there is a clear and substantial variation of the peaks at the M -points from one Brillouin zone

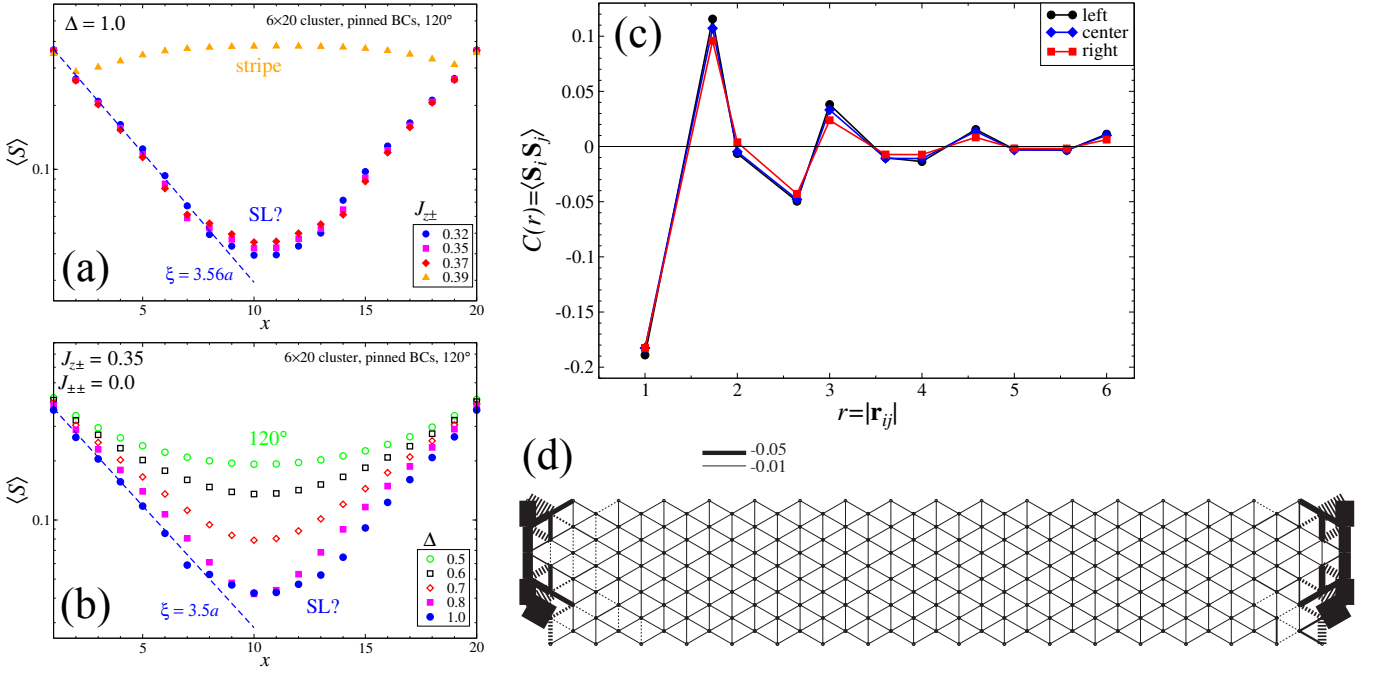


FIG. 11: (a) and (b) $\langle S \rangle$ vs the length of the cylinder in the 6×20 clusters with the 120° boundary conditions on a semi-log plot. The exponential decay in the spin-liquid state with the correlation length ξ is emphasized. (a) is for $\Delta = 1.0$, $J_{\pm\pm} = 0$ for several $J_{z\pm}$. (b) is for $J_{\pm\pm} = 0$, $J_{z\pm} = 0.35$ for several values of Δ . (c) The real space spin-spin correlation function, $C(r) = \langle \mathbf{S}_i \mathbf{S}_j \rangle$, with $r = |\mathbf{r}_{ij}|$ in the three sections of Fig. 5(a) of the main text. (d) The 1D scan from Fig. 5(a) of the main text showing magnified bonds of $\langle \mathbf{S}_i \mathbf{S}_j \rangle + 0.175$.

to the other. We note that the latter feature has been clearly observed in the neutron-scattering experiments in YMGO [11], yielding a yet more support to the disordered stripe state scenario [5].

Lastly, we suggest that the polarized neutron scattering may be able to identify contribution of the off-diagonal $\mathcal{S}(\mathbf{q})$ components in YMGO.

Correlations and other orders

Correlation length.—For the suspected spin-liquid region of the model (1) and (2), we have measured the decay of the ordered moment $\langle S \rangle$ away from the boundaries in the 6×20 clusters with the 120° boundary conditions. In the spin-liquid state, such decays are always exponential with the correlation length about 3 – 4 lattice spacings, see Fig. 11(a) and (b). The first plot shows the ordered moment $\langle S \rangle$ vs the length of the cylinder on a semi-log plot to emphasize the exponential form of the decay. It is for fixed $\Delta = 1.0$ and $J_{\pm\pm} = 0$ and for several values of $J_{z\pm}$ from the spin-liquid region with one set from the neighboring stripe phase for a contrast. The second panel shows the same type of data for $J_{\pm\pm} = 0$ and $J_{z\pm} = 0.35$ and for several values of Δ , also confirming the results in Fig. 8 that a transition from the 120° order to an SL state is near $\Delta \sim 0.7 - 0.8$.

This is yet another type of measurement that we use to confirm the existence of the spin-liquid phase. One of the

problems with using it to identify the extent of a spin-liquid phase is that the decay is still exponential when the order is weak but is certainly present, thus leading to an overestimate of such a region.

Correlation function of the spin-liquid state.—In addition to the structure factor $S(\mathbf{q})$ above, we provide further support to the isomorphism of the spin-liquid phase throughout J_1 – J_2 – $J_{z\pm}$ parameter space, by investigating the real space spin-spin correlation function, $C(r) = \langle \mathbf{S}_i \mathbf{S}_j \rangle$, where $r = |\mathbf{r}_{ij}|$. We have chosen the same three regions of the spin-liquid phase in the “spin-liquid cylinder” of Fig. 5 of the main text [also shown in Fig. 9], for which we had the nearly identical $S(\mathbf{q})$ maps.

The results for $C(r)$ for three different sections of the cylinder, marked “left,” “center,” and “right,” are shown in Fig. 11(c). The correlations are measured, roughly, along the diagonal of each of the section and reach the distances $r = 6a$ that corresponds to the 11th nearest-neighbor. One can plainly see that even the fine structure of the correlations is the same, e.g., showing a near-zero correlation for the third neighbor, and that $C(r)$ ’s remain quantitatively close all the way from the anisotropic spin-liquid to the isotropic J_1 – J_2 one. Therefore, according to our measurements, with the accuracy one can detect, the “anisotropic” spin liquid and “isotropic” spin liquids are the same, or isomorphic to each other.

Valence-bond and chiral orders.—Although we have not observed any indication of the dimerized states in

any of our scans [the thickness of the bonds in all our cylinders is proportional to the nearest-neighbor correlation $\langle \mathbf{S}_i \mathbf{S}_j \rangle$], we have also conducted a direct search for possible dimerization patterns, see Fig. 11(d). This Figure shows the same 1D “spin-liquid cylinder” scan as in Fig. 5(a) of the main text and above with the value -0.175 subtracted from the nearest-neighbor correlation $\langle \mathbf{S}_i \mathbf{S}_j \rangle$ (the average value of it is about -0.18). The result of the subtraction is magnified to make the subtler variations visible on the scale of 0.01 or less. Aside from the open-boundary-related effects, no sign of a dimerization pattern is detected.

For the same 1D scan, we have searched for a non-zero chirality by measuring $\langle \mathbf{S}_1 (\mathbf{S}_2 \times \mathbf{S}_3) \rangle$ on each triangle and found that the chirality values are less than 10^{-8} , i.e., beyond detectability.

-
- [1] Y. Li, G. Chen, W. Tong, Li Pi, J. Liu, Z. Yang, X. Wang, and Q. Zhang, Phys. Rev. Lett. **115**, 167203 (2015).
 - [2] C. Liu, X. Wang, R. Yu, Phys. Rev. B **94**, 174424 (2016).
 - [3] Q. Luo, S. Hu, B. Xi, J. Zhao, and X. Wang, Phys. Rev.

- B **95**, 165110 (2017).
- [4] A. Biffin, R. D. Johnson, I. Kimchi, R. Morris, A. Bombardi, J. G. Analytis, A. Vishwanath, and R. Coldea, Phys. Rev. Lett. **113**, 197201 (2014).
- [5] Z. Zhu, P. A. Maksimov, S. R. White, and A. L. Chernyshev, Phys. Rev. Lett. **119**, 157201 (2017).
- [6] Y.-D. Li, Y. Shen, Y. Li, J. Zhao, and G. Chen, arXiv:1608.06445.
- [7] S. Tóth, K. Rolfs, A. R. Wildes, and C. Rüegg, arXiv:1705.05699.
- [8] J. A. M. Paddison and M. Mourigal, private communication.
- [9] Z. Zhu and S. R. White, Phys. Rev. B **92**, 041105 (2015).
- [10] S. R. White and A. L. Chernyshev, Phys. Rev. Lett. **99**, 127004 (2007).
- [11] J. A. M. Paddison, M. Daum, Z. Dun, G. Ehlers, Y. Liu, M. B. Stone, H. Zhou, and M. Mourigal, Nat. Phys. **13**, 117 (2017).
- [12] Y. Shen, Y.-D. Li, H. Wo, Y. Li, S. Shen, B. Pan, Q. Wang, H. C. Walker, P. Steffens, M. Boehm, Y. Hao, D. L. Quintero-Castro, L. W. Harriger, M. D. Frontzek, L. Hao, S. Meng, Q. Zhang, G. Chen, and J. Zhao, Nature **540**, 559 (2016).
- [13] J. Iaconis, C. Liu, G. B. Halász, and L. Balents, arXiv:1708.07856.